Prediction of the speciation of alkaline earths adsorbed on mineral surfaces in salt solutions

Dimitri A. Sverjensky *

Department of Earth and Planetary Sciences, The Johns Hopkins University, Baltimore, MD 21218, USA

Received 5 August 2005; accepted in revised form 11 January 2006

Abstract

Despite the fact that the bulk compositions of most low temperature natural surface waters, groundwaters, and porewaters are heavily influenced by alkaline earths, an understanding of the development of proton surface charge in the presence of alkaline earth adsorption on the surfaces of minerals is lacking. In particular, models of speciation at the mineral–water interface in systems involving alkaline earths need to be established for a range of different minerals. In the present study, X-ray standing wave results for Sr^{2+} adsorption on rutile as a tetranuclear complex [Fenter, P., Cheng, L., Rihs, S., Machesky, M., Bedyzk, M.D., Sturchio, N.C., 2000. Electrical double-layer structure at the rutile–water interface as observed in situ with small-period X-ray standing waves. *J. Colloid Interface Sci.* **225**, 154–165] are used as constraints for all the alkaline earths in surface complexation simulations of proton surface charge, metal adsorption, and electrokinetic experiments referring to wide ranges of pH, ionic strength, surface coverage, and type of oxide. The tetranuclear reaction

$$4 > SOH + M^{2+} + H_2O = (> SOH)_2(> SO^-)_2\_M(OH)^+ + 3H^+$$

predominates for the large cations Sr^{2+} and Ba^{2+} (and presumably Ra^{2+}), consistent with X-ray results. In contrast, the mononuclear reaction
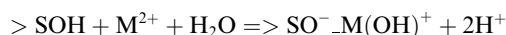
$$> SOH + M^{2+} + H_2O => SO^-\_M(OH)^+ + 2H^+$$

predominates for the much smaller Mg^{2+} (and presumably Be^{2+}), with minor amounts of the tetranuclear reaction. Both reaction types appear to be important for the intermediate size Ca^{2+}. For all the alkaline earths on all oxides, the proportions of the different reaction types vary systematically as a function of pH, ionic strength, and surface coverage.

The application of Born solvation and crystal–chemical theory enables estimation of the equilibrium constants of adsorption of all the alkaline earths on all oxides. On high dielectric constant solids (rutile, magnetite, manganese dioxide), where the solvation contribution is negligable, ion adsorption correlates with crystal radius: the equilibrium constants increase in the sequence $Be^{2+} < Mg^{2+} < Ca^{2+} < Sr^{2+} < Ba^{2+} < Ra^{2+}$. On low dielectric constant solids (hematite, gibbsite, and silicas), the solvation contribution opposing adsorption is largest for ions with the smallest hydrated radii: the equilibrium constants increase in the sequence $Ra^{2+} < Ba^{2+} < Sr^{2+} < Ca^{2+} < Mg^{2+} < Be^{2+}$. These predicted sequences are consistent with adsorption affinities in the literature. In combination with previously published results, the present study enables the predictive use of the triple-layer model for 1:1 and 2:1 electrolytes, and mixtures of these, permitting calculation of proton surface charge and adsorption under conditions more relevent to natural water compositions than previously possible.
© 2006 Elsevier Inc. All rights reserved.

---

* Fax: +1 410 516 7933.
  E-mail address: sver@jhu.edu.

1. Introduction

The bulk compositions of most low temperature natural surface waters, groundwaters and porewaters are heavily influenced by alkaline earths (Drever, 1997). For example, rivers and groundwaters often consist of Ca-Na-HCO$_3$-SiO$_2$ species and the oceans consist of Na-Mg-Cl-SO$_4$ species. Reactions between these types of waters and mineral surfaces should be greatly influenced by the alkaline earths. For example, the immersion of minerals in alkaline earth electrolytes strongly enhances proton surface charge relative to 1:1 electrolytes (Davis et al., 1978; Yates et al., 1980; Jang and Fuerstenau, 1986; Ridley et al., 1999, 2004; Karlsson et al., 2001; Rietra et al., 2001). Despite this evidence, most experimental studies of the mineral–water interface have focussed on the use of simple 1:1 electrolytes (e.g., NaNO$_3$, NaClO$_4$) which have limited relevence to natural waters. As a consequence, surface complexation models of the mineral–water interface restricted to fitting experimental data for 1:1 electrolytes cannot be used to make predictions for systems containing alkaline earth electrolytes. In particular, the speciation at the mineral–water interface in systems involving alkaline earths needs to be established.

The nature of the metal species adsorbed to mineral surfaces is a topic that has received considerable attention from a wide variety of experimental and theoretical standpoints (Schindler and Stumm, 1987; Davis and Kent, 1990; Stumm, 1992; Venema et al., 1996; Brown and Parks, 2001; Zhang et al., 2004b). It is the precise way in which a metal is bonded to a surface through one or more surface sites and whether it is also bonded to species other than water, such as hydroxyl or other anions, that determines the stoichiometry of the adsorption reaction, which in turn controls the extent of adsorption and its dependence on other variables such as pH, ionic strength, surface coverage, and type of electrolyte (Hayes and Leckie, 1986; Criscenti and Sverjensky, 1999; Criscenti and Sverjensky, 2002). The most definitive evidence for the nature of metal surface species has come from a variety of synchrotron-based X-ray techniques (Brown and Sturchio, 2002). In particular, the advent of the application of X-ray standing wave techniques to the rutile–water interface in situ has resulted in an extremely detailed picture of the nature of several adsorbed cations, including an alkaline earth (Fenter et al., 2000; Zhang et al., 2004a,b).

X-ray standing wave studies of Sr^{2+}, Y^{3+}, Zn^{2+}, and Rb$^+$ in salt solutions at the rutile (110) surface demonstrate two important features of cation adsorption (Zhang et al., 2004a,b). First, divalent cations with different sizes (e.g., Sr^{2+} and Zn^{2+}) form different adsorbed species. Second, a given cation (Zn^{2+}) can form more than one type of adsorbed species. These results for just one surface plane on one solid clearly indicate the potential chemical complexity of cation surface speciation. More than one type of metal surface species in a given system has also been reported in other synchrotron-based X-ray studies of powders and single crystal surfaces (Spadini et al., 1994; Bargar et al., 1997c; Cheah et al., 1998; Ostergren et al., 2000; Waychunas et al., 2002; Auwer et al., 2003; Trivedi et al., 2003; Zhang et al., 2004a,b), as well as in electron paramagnetic resonance (Hyun et al., 2003) and fluorescence spectroscopic studies (Gabriel et al., 2001). More indirect model-dependent evidence of the same result has arisen in surface complexation studies of the adsorption of metals on powders immersed in electrolyte solutions (Gunneriusson and Sjöberg, 1993; Criscenti and Sverjensky, 2002). The existence of more than one metal surface species in a given system clearly necessitates examining metal adsorption under wide ranges of conditions to attempt to unravel the conditions under which different species predominate.

From an experimental standpoint, the most elusive aspect of metal surface species is their state of bonding to water, hydroxyl, or other anions. Despite progress in the application of synchrotron-based X-ray techniques, the results do not yield direct experimental evidence of the state of protonation of surface metal species. Theoretical bond valence methods have been developed to attempt to predict the protonation state of metal surface species (Bargar et al., 1997a,b; Ostergren et al., 2000). However, molecular dynamics and quantum mechanical studies indicate that the attribution of charge to individual species using bond valence methods may be too simplistic (Felmy and Rustad, 1998; Predota et al., 2004a,b). An alternate approach is to recognize that the number of hydroxyl anions bonded to the surface metal species directly affects the stoichiometry of the metal adsorption reactions and the form of the electrostatic work term in the equilibrium constant expression in surface complexation models. This in turn directly affects the predicted behavior of metal adsorption as a function of pH, ionic strength, and surface coverage. It is here that surface complexation models are of use for distinguishing between alternate speciation schemes.

Surface complexation models include the stoichiometry of metal adsorption reactions that specify a protonation state for one or more metal surface species. By simulating adsorption reactions over wide ranges of pH, ionic strength, electrolyte type, and surface coverage, the predicted proton and/or metal uptake can be directly compared to experimental data. Ideally, several different types of experimental data should be used, including studies of metal adsorption, and proton surface charge and electrokinetics in the presence of metals. However, few surface complexation studies have attempted to integrate all these types of experimental data (James et al., 1981; Charmas et al., 2002; Prélot et al., 2002; Boily et al., 2005). It should be emphasized here that what is being determined is one or more reaction stoichiometries. In contrast, X-ray studies yield information on the nature of the metal surface species themselves, which helps constrain the selection of adsorption reactions. The technique of surface complexation modelling is therefore complementary to X-ray techniques. Unfortunately, the number of surface complexation studies which attempt to integrate the constraints derived from

X-ray studies with simulations of proton and metal uptake are very few (Venema et al., 1997; Spadini et al., 2003; Dyer et al., 2004; Peacock and Sherman, 2004; Ridley et al., 2004; Boily et al., 2005).

In the present study, the X-ray standing wave studies of Sr^{2+} are used as constraints for all the alkaline earths in surface complexation simulations of proton surface charge, metal adsorption, and electrokinetic experiments. Emphasis is placed on experiments referring to a wide range of pH, ionic strength, surface coverage, and types of solids. The goals of the simulations are to determine whether or not more than one reaction stoichiometry is needed, the state of protonation of the metal surface species, and whether different minerals share common reaction stoichiometries. Previous surface complexation studies have demonstrated that if a wide enough range of conditions are considered, e.g., wide ranges of pH, ionic strength, and surface coverage, it is possible to constrain reaction stoichiometries (James et al., 1981; Criscenti and Sverjensky, 1999, 2002). The overall goal of the present study is to develop a predictive framework for the equilibrium constants corresponding to metal adsorption reactions, guided by the application of Born solvation and crystal–chemical theory (Sverjensky, 1993, 1994, 2001, 2003; Sahai and Sverjensky, 1997a,b). To be able to make predictions for systems not yet studied experimentally, or to be able to extend experimental observations made over a limited range of conditions, is a goal that has rarely been attempted in studies of the mineral–water interface (Dzombak and Morel, 1990; Sverjensky, 2005).

Previous surface complexation studies of alkaline earths have focussed on only one or two members of the family (James and Healy, 1972; Vuceta, 1976; Balistrieri and Murray, 1981; Kent and Kastner, 1985; Chen and Hayes, 1999; Ridley et al., 1999, 2004; O'Day et al., 2000; Sahai et al., 2000; Zhang et al., 2004b), or on only a single solid (Ahmed and Cleave, 1965; Tadros and Lyklema, 1969; Jang and Fuerstenau, 1986; Dzombak and Morel, 1990; Kosmulski, 1994; Ali and Dzombak, 1996; Axe et al., 1998; Chen and Hayes, 1999; Kitamura et al., 1999; Rietra et al., 2001; Weng et al., 2005). In the present study, consideration of a wide range of alkaline earths and solids facilitates establishing whether or not there are surface reactions common to all the alkaline earths and oxides. If so, it becomes possible to examine systematic changes in alkaline earth adsorption that facilitate prediction for systems lacking data.

2. Analysis of adsorption, proton charge, and electrokinetic data

2.1. Modelling approach, assumptions, and uncertainties

2.1.1. Surface complexation approach

The approach used in the present study builds on the single-site triple-layer model and crystal–chemical and Born solvation theory, referred to as the extended triple-layer model (ETLM). As described previously (Sverjensky and Sahai, 1996; Sahai and Sverjensky, 1997a,b; Sverjensky, 2001, 2005), this approach has resulted in a predictive model for proton surface charge development in 1:1 electrolytes. A single-site surface complexation model is used because, with the exception of a single study (Fenter et al., 2000), all the available experimental data for metal adsorption on oxides refer to powders immersed in salt solutions. The data consequently consist of an averaging over many crystal planes and different sites. Such averaging is conveniently treated with a single-site model. As new experimental data on powders are obtained they serve as a test of the model predictions. The triple-layer model is used here because it has a level of complexity required to account for a range of electrolyte types and concentrations.

A critical feature of the approach taken below is that experimental studies of proton surface charge, adsorption, and electrokinetic data referring to wide ranges of pH, ionic strength, surface coverage, and type of mineral are analyzed. Second, the results of this analysis are interpreted and correlated with the aid of solvation, crystal–chemical, and thermodynamic theory. In this way, the equilibrium constants for metal adsorption can be placed on a predictive basis. The purpose of developing the ETLM with solvation and crystal–chemical theory is that predictions of alkaline earth adsorption or effects on surface charge can be made for conditions that have not been investigated experimentally.

Recent advances in the definition and interpretation of standard states for the thermodynamic activities of surface sites and species facilitate an accurate comparison of the equilibrium constants for alkaline earth adsorption for different samples of the same solid, as well as for samples of different solids (Sverjensky, 2003, 2005). In the present study, attention is focussed on developing the ETLM consistent with these standard states (Appendix A). Sample characteristics and the necessary parameters for implementing the standard states, as well as for computing surface protonation in the presence of 1:1 electrolyte adsorption in the present study are given in Table 1.

2.1.2. Surface complexation assumptions

Following previous studies of metal adsorption using the triple-layer model (Davis and Leckie, 1978; James et al., 1981; Hayes and Leckie, 1986; Hayes and Leckie, 1987; Criscenti and Sverjensky, 1999; Criscenti and Sverjensky, 2002), it is assumed that the metal adsorbs to either the 0, β, or d planes of the model. This assumption, together with the reaction stoichiometry, determines the magnitude of the electrostatic work term associated with the reaction. In contrast, in the three-plane CD-model (Hiemstra and van Riemsdijk, 1996), it is assumed that the charge of the adsorbing metal is distributed between the 0 plane (where protons adsorb) and the 1 planes according to a fraction (f) associated with each adsorbed metal species (Venema et al., 1996; Rietra et al., 2001; Weng et al., 2005). In practise, the f value often becomes an additional

Table 1
Sample characteristics and triple-layer model parameters for proton and 1:1 electrolyte adsorption

Solid	Salt (ML)	N_s (sites nm^{-2})	A_s (m^2 g^{-1})	pH$_{ZPC}$	ΔpK_n^θ	$\log K_1^\theta$	$\log K_2^\theta$	$\log{}^*K_{M^+}^\theta$	$\log{}^*K_{L^-}^\theta$	C_1 (μF cm^{-2})	Source of the surface charge data
α-TiO$_2$	NaCl	12.5	17.0	5.4[d]	6.3	2.2	8.6	−6.1	4.5	120	Machesky et al. (1998)[a]
α-TiO$_2$	KNO$_3$	12.5	20.6	5.9[e]	6.3	2.8	9.1	−6.3	5.1	90	Jang and Fuerstenau (1986)[b]
α-TiO$_2$	KNO$_3$	12.5	20.0	5.8[e]	6.3	2.6	9.0	−6.9	4.8	110	Yates (1975)[a]
α-FeOOH	NaCl	16.4	79.4	8.3[f]	5.6	5.2	10.8	−8.6	7.2	115	Ali (1994)[a]
α-FeOOH	NaCl	16.4	51.8	7.6[g]	5.6	4.8	10.4	−8.8	6.4	90	Balistrieri and Murray (1981)[b]
γ-Al$_2$O$_3$	NaCl	8.0	100.0	8.65[e]	5.9	5.8	11.7	−9.0	8.0	90	Huang and Stumm (1973)[a]
α-SiO$_2$	NaCl	4.5	4.15	3.0[e]	8.4	−1.2	7.2	−6.5	−0.5[j]	100	Riese (1983)[a]
α-SiO$_2$	KNO$_3$	11.4	4.2	1.2[h]	8.4	−2.2	6.2	−4.2	−0.2[j]	60	Vuceta (1976)[c]
am. SiO$_2$	NaCl	4.6	388	2.8[i]	8.4	−1.4	7.0	−7.4	−1.8[j]	95	Kosmulski (1994)[c]
am. SiO$_2$	NaCl	4.6	131.2	2.8[i]	8.4	−1.4	7.0	−6.9	−1.3[j]	105	Kent and Kastner (1985)[c]

The model parameters $\log{}^*K_{M^+}^0$, $\log{}^*K_{L^-}^0$, and C_1 were generated by regression of proton surface charge data[a,b] or predicted[c]. Values of N_s and ΔpK_n^θ were taken from Sverjensky (2005) unless otherwise noted. Values of A_s are BET surface areas from the sources listed. Values of pH$_{ZPC}$ refer to low ionic strength isoelectric points[d], values of pH$_{PZSE}$ corrected for electrolyte ion adsorption effects as noted (see also text), or theoretical predictions[e]. Values of $\log K_1^\theta$ and $\log K_2^\theta$ were calculated from the values of pH$_{ZPC}$ and ΔpK_n^θ. The equilibrium constants listed refer to reactions given in the appendix.
  [a] Regression of proton surface charge data reported in Sverjensky (2005).
  [b] Regression of proton surface charge data in the present study.
  [c] Parameters predicted from equations in Sverjensky (2005).
  [d] Point of zero salt effect from Machesky et al. (1998). Correction for effect of electrolyte is negligable.
  [e] Low ionic strength isoelectric point from the source of the surface charge data given in the table.
  [f] Calculated from experimental pH$_{PZSE}$ = 8.2 (Ali, 1994) using Eq. (31).
  [g] Calculated from experimental pH$_{PZSE}$ = 7.5 (Balistrieri and Murray, 1981) using Eq. (31).
  [h] Calculated assuming that $\log K_{>SO^-\_Ca(OH)^+}^\theta$, for Vuceta (1976) is the same as that derived from the data of Riese (1983).
 [i] Theoretically predicted value (Sverjensky, 2005).
  [j] Estimated based on the zpc and $\log{}^*K_{M^+}^0$.

fit parameter (c.f. different f values for Ca on goethite in Rietra et al., 2001 versus Weng et al., 2005). For each metal surface species this results in two fit parameters, i.e., a log K value and an f value. Given the strong likelihood of multiple surface species, this can rapidly result in numerous fit parameters. As a consequence, the model becomes insensitive to whether one or more than one metal surface reaction is used (e.g., Rietra et al., 2001). In addition, because the adsorption data typically refers to powders rather than single crystals, assumptions, or model fits to data, are required to establish the proportions of different crystallographic planes contributing to the overall adsorption (e.g., Venema et al., 1996). Under these circumstances, it becomes extremely difficult to develop a model that can be used for prediction in the absence of experimental data. An alternate approach, placing the adsorbing metal on it's own plane between the 0 plane and the plane where electrolyte ions adsorb (Ridley et al., 2004) also results in an additional fitting parameter, the capacitance between the 0 plane and the plane of the metal ion. Such capacitances for calcium on rutile are very large (393–613 μF cm^{-2}) and may be difficult to estimate for predictive purposes (see below).

In the present study, it was found that placing the alkaline earths on the β plane accounted for almost all the data. It should be emphasized that this does not, a priori, imply that the model complexes are outer sphere (Sverjensky, 2001, 2005). Model values of the distance β on high dielectric constant oxides such as rutile, consistent with X-ray studies (Fenter et al., 2000) and molecular calculations

(Predota et al., 2004a,b), indicate that model β-plane surface complexes on such solids can indeed be inner sphere. In contrast, on low dielectric constant solids such as silica, the larger values of β indicate the likelihood of outer-sphere complexes. Consequently, the present study does not explicitly account for inner- vs. outer-sphere complexes in the way the reactions are modeled. Instead, it is suggested that the likelyhood of inner- vs. outer-sphere can be inferred from the distance β. It will be shown below that in a few instances of alkaline earth adsorption, a d-plane complex was required by the adsorption data. It seems likely that in such instances the model surface complexes should be interpreted as outer sphere.

It is further assumed in the present study that two or more species of adsorbed metal can occur in the model, particularly when very large ranges of pH, ionic strength, and surface coverage are involved. If the corresponding adsorption reactions are sufficiently different, the need for such species can be clearly distinguished. For example, as originally demonstrated by Davis and Leckie (1978), the reaction

$$> SOH + M^{2+} => SO^-\_M^{2+} + H^+, \qquad (1)$$
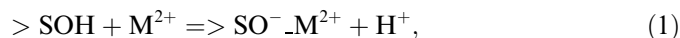
where

$$^*K_{>SO^-\_M^{2+}}^\theta = \left(\frac{a_{>SO^-\_M^{2+}} a_{H^+}}{a_{>SOH} a_{M^{2+}}} \right) 10^{\frac{F(2\psi_\beta - \psi_0)}{2.303RT}} \qquad (2)$$
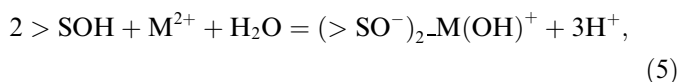
can be distinguished from the reaction

$$> SOH + M^{2+} + H_2O => SO^-\_M(OH)^+ + 2H^+, \qquad (3)$$

where

$$*K^\theta_{>SO^-\_M(OH)^+} = \left(\frac{a_{>SO^-\_M(OH)^+} a^2_{H^+}}{a_{>SOH} a_{M^{2+}} a_{H_2O}}\right) 10^{\frac{F(\psi_\beta - \psi_0)}{2.303RT}}. \quad (4)$$

In Eqs. (2) and (4), and subsequent equations, the superscript "*" represents a reaction expressed relative to the species >SOH and the superscript "θ" represents site occupancy standard states (Appendix A). It can be seen in Eqs. (2) and (4) that the mass action and electrostatic factors are different, which results in contrasting model behavior for metal adsorption as functions of pH, ionic strength, and surface coverage.

However, the adsorption reaction

$$2 > SOH + M^{2+} + H_2O = (> SO^-)_2\_M(OH)^+ + 3H^+, \quad (5)$$

where

$$*K^\theta_{(>SO^-)_2\_M(OH)^+} = \left(\frac{a_{(>SO^-)_2\_M(OH)^+} a^3_{H^+}}{a^2_{>SOH} a_{M^{2+}} a_{H_2O}}\right) 10^{\frac{F(\psi_\beta - 2\psi_0)}{2.303RT}} \quad (6)$$

cannot be so easily distinguished from the reaction

$$4 > SOH + M^{2+} + H_2O = (> SOH)_2(> SO^-)_2\_M(OH)^+ + 3H^+, \quad (7)$$
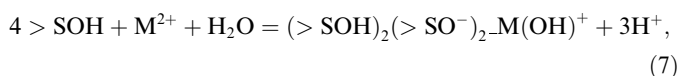
where

$$*K^\theta_{(>SOH)_2(>SO^-)_2\_M(OH)^+} = \left(\frac{a_{(>SOH)_2(>SO^-)_2\_M(OH)^+} a^3_{H^+}}{a^4_{>SOH} a_{M^{2+}} a_{H_2O}}\right) 10^{\frac{F(\psi_\beta - 2\psi_0)}{2.303RT}} \quad (8)$$

because the mass action expressions are so similar and the electrostatic factors are identical. Adsorption data over a wide range of surface coverages would be needed.

Recent X-ray standing wave results for the adsorption of Sr^{2+} on the (110) surface of rutile (Fenter et al., 2000; Zhang et al., 2004a,b) have established that Sr^{2+} is coordinated to four surface oxygens, comprised of two bridging and two terminal oxygen species (the state of protonation not being determinable by X-ray methods). In the present study, it will be assumed that this result for Sr^{2+} can be approximated by the surface species $(>SOH)_2(>SO^-)_2\_M(OH)^+$ or $(>SOH)_2(>SO^-)_2\_M^{2+}$, where M^{2+} stands for any of the alkaline earths. It was found that adsorption reactions corresponding to one or both of these species proved extremely useful for parts of the ranges of pH, ionic strength, and surface coverage investigated. For other conditions, additional species were required, depending on the mineral involved.

2.1.3. Uncertainties in experimental data and model equilibrium constants

The assessment of uncertainties in individual experimental datasets for proton surface charge, metal adsorption or electrokinetic results is often not provided. For proton surface charge studies on a series of identical suspensions an uncertainty of $\pm 0.5~\mu C~cm^{-2}$ has been cited (Yates et al.,

1980). Unless otherwise stated, these uncertainties have been used as a guide in the analysis discussed below, resulting in an overall uncertainty for the log K of about ± 0.3.

2.1.4. Regression procedure and types of equilibrium constants generated

Regression of the proton surface charge and adsorption data discussed below generated values of the equilibrium constants for alkaline earth adsorption represented by $\log^* K^0_M$ (Table 2). The superscript "0" here represents the hypothetical 1.0 M standard state (Appendix A). The values of $\log^* K^0_M$ were converted to site-occupancy standard states, i.e., $\log K^\theta_M$, referring to the reactions producing the surface species from $>SO^-$ and OH^- using equations summarized below and given in the Appendix A, together with the values of N_s (site density), A_s (BET surface area), C_s (solid concentration), pH_{ZPC}, and ΔpK^θ_n given in Table 2. It is the $\log K^\theta_M$ equilibrium constants which are independent of the individual sample characteristics, and therefore useful for comparing the dependence of akaline earth adsorption on different oxides. These differences are analyzed below. The $\log K^\theta_M$ equilibrium constants for different oxides are regressed with the aid of Born solvation theory to calibrate predictive equations for alkaline earth adsorption on all oxides.

2.2. Alkaline earths on rutile

2.2.1. Ca on rutile from Ridley et al. (1999)

Experimental data for the adsorption of Ca on rutile in NaCl solutions and the proton surface charge in NaCl solutions in the presence of Ca are represented by the symbols in Fig. 1. The results of different runs for proton surface charge (represented by the different symbols for a given ionic strength) suggest that the overall uncertainties at the highest pH values may be of the order of $\pm 3~\mu C~cm^{-2}$. During the course of the measurements depicted by the symbols, the pH was changed by the addition of sufficient titrant to cause a progressive dilution of the initial Ca concentration from 0.001 to about 0.0007 M. As a consequence, the data sets do not represent constant overall Ca or solid concentrations. In the present study, in order to facilitate the computation of model curves and equilibrium constants, a uniform set of Ca and solid concentrations were adopted as noted on the figures. These values were chosen to reflect the steepest most rapidly changing parts of the data. This approach is an approximation only, but it nevertheless yielded equilibrium constants close to the ones obtained by fitting the data for Ca proton surface charge from Jang and Fuerstenau (1986) in Fig. 2 (see below).

The four solid curves depicted on the left-hand side of Fig. 1 represent regression calculations using the adsorption reactions producing $(>SOH)_2(>SO^-)_2\_Ca(OH)^+$ and $>SO^-\_Ca(OH)^+$ (Table 2). It should be emphasized that the data in Fig. 1, by themselves, do not require the choice of these specific surface complexes. Instead, the

Table 2
Equilibrium constants for alkaline earth adsorption

Solid	M	$\log {}^*K_M^0$	Surface species	N_s	A_s	C_s	pH_{ZPC}	ΔpK_n^θ	$\log K_M^\theta$
α-TiO$_2$[a]	Ca	−10.4	$4>SOH + M^{2+} + H_2O = (>SOH)_2 (>SO^-)_2\_M(OH)^+ + 3H^+$	12.5	17.0	31.0	5.4	6.3	32.5
	Ca	−11.4	$>SOH + M^{2+} + H_2O = >SO^-\_M(OH)^+ + 2H^+$	12.5	17.0	31.0	5.4	6.3	11.5
α-TiO$_2$[b]	Mg	−12.7	$4>SOH + M^{2+} + H_2O = (>SOH)_2 (>SO^-)_2\_M(OH)^+ + 3H^+$	12.5	20.6	20.0	5.9	6.3	31.0
	Mg	−12.5	$>SOH + M^{2+} + H_2O = >SO^-\_M(OH)^+ + 2H^+$	12.5	20.6	20.0	5.9	6.3	11.0
	Ca	−11.2	$4>SOH + M^{2+} + H_2O = (>SOH)_2 (>SO^-)^+\_M(OH)^+ + 3H^+$	12.5	20.6	20.0	5.9	6.3	32.5
	Ca	−12.0	$>SOH + M^{2+} + H_2O = >SO^-\_M(OH)^+ + 2H^+$	12.5	20.6	20.0	5.9	6.3	11.5
	Sr	−10.4	$4>SOH + M^{2+} + H_2O = (>SOH)_2 (>SO^-)^+\_M(OH)^+ + 3H^+$	12.5	20.6	20.0	5.9	6.3	33.3
	Sr	−11.9	$>SOH + M^{2+} + H_2O = >SO^-\_M(OH)^+ + 2H^+$	12.5	20.6	20.0	5.9	6.3	11.5
	Ba	−9.2	$4>SOH + M^{2+} + H_2O = (>SOH)_2 (>SO^-)^+\_M(OH)^+ + 3H^+$	12.5	20.6	20.0	5.9	6.3	34.5
	Ba	−11.5	$>SOH + M^{2+} + H_2O = >SO^-\_M(OH)^+ + 2H^+$	12.5	20.6	20.0	5.9	6.3	12.0
α-FeOOH[c]	Ca	−6.4	$4>SOH + M^{2+} = (>SOH)_2 (>SO^-)_2\_M^{2+} + 2H^+$	16.4	79.4	1.6	8.4	5.6	27.1
	Ca	−16.4	$4>SOH + M^{2+} + H_2O = (> SOH)_2 (>SO^-)^+\_M(OH)^+ + 3H^+$	16.4	79.4	1.6	8.4	5.6	31.1
	Ca	−16.5	$>SOH + M^{2+} + H_2O = >SO^-\_M(OH)^+ + 2H^+$	16.4	79.4	1.6	8.4	5.6	9.8
α-FeOOH[d]	Mg	−7.9	$4>SOH + M^{2+} = (>SOH)_2 (>SO^-)_2\_M^{2+} + 2H^+$	16.4	51.8	7.43	7.6	5.6	25.2
	Mg	−15.3	$>SOH + M^{2+} + H_2O = >SO^-\_M(OH)^+ + 2H^+$	16.4	51.8	7.43	7.6	5.6	9.9
	Mg	−14.0	$4>SOH + M^{2+} + Cl^- + H_2O = (>SOH)_2 (>SO^-)_2\_M(OH)Cl + 3H^+$	16.4	51.8	7.43	7.6	5.6	33.1
	Ca	−7.1	$4>SOH + M^{2+} = (>SOH)_2 (>SO^-)^2\_M^{2+} + 2H^+$	16.4	51.8	7.43	7.6	5.6	26.0
α-FeOOH[e]	Ba	−19.3	$4>SOH + M^{2+} + H_2O = (>SOH)_2 (>SO^-)_2\_M(OH)^+ + 3H^+$	16.4	52.0	30.0	8.6	5.6	31.7
	Ba	−1.8	$4>SOH + M^{2+} + H_2O = (>SOH)_4\_M(OH)^+ + H^+$	16.4	52.0	30.0	8.6	5.6	12.4
	Ba	−17.5	$4>SOH + M^{2+} + NO^-_3 + H_2O = (>SOH)_2 (>SO^-)_2\_M(OH)^+ + 3H^+$	16.4	52.0	30.0	8.6	5.6	33.5
γ-Al$_2$O$_3$[f]	Mg	−16.3	$>SOH + M^{2+} + H_2O = >SO^-\_M(OH)^+ + 2H^+$	8.0	117.0	3.23	8.65	5.9	10.3
	Mg	−16.0	$4>SOH + M^{2+} + H_2O = (>SOH)_2 (>SO^-)^+\_M(OH)^+ + 3H^+$	8.0	117.0	3.23	8.65	5.9	32.6
	Mg	−7.7	$4>SOH + M^{2+} = (>SOH)_2 (>SO^-)_2\_ M^{2+} + 2H^+$	8.0	117.0	3.23	8.65	5.9	26.9
	Ca	−16.8	$>SOH + M^{2+} + H_2O = >SO^-\_M(OH)^+ + 2H^+$	8.0	117.0	3.23	8.65	5.9	9.8
	Ca	−17.6	$4>SOH + M^{2+} + H_2O = (>SOH)_2 (>SO^-)^+\_M(OH)^+ + 3H^+$	8.0	117.0	3.23	8.65	5.9	30.8
	Ca	−8.2	$4>SOH + M^{2+} = (>SOH)_2 (>SO^-)_2\_ M^{2+} + 2H^+$	8.0	117.0	3.23	8.65	5.9	26.4
	Sr	−17.3	$>SOH + M^{2+} + H_2O = >SO^-\_M(OH)^+ + 2H^+$	8.0	117.0	3.23	8.65	5.9	9.3
	Sr	−18.4	$4>SOH + M^{2+} + H_2O = (>SOH)_2 (>SO^-)^+\_M(OH)^+ + 3H^+$	8.0	117.0	3.23	8.65	5.9	30.2
	Sr	−8.2	$4>SOH + M^{2+} = (>SOH)_2 (>SO^-)_2\_ M^{2+} + 2H^+$	8.0	117.0	3.23	8.65	5.9	26.4
	Ba	−19.0	$4>SOH + M^{2+} + H_2O = (>SOH)_2 (>SO^-)^+\_M(OH)^+ + 3H^+$	8.0	117.0	3.23	8.65	5.9	29.6
	Ba	−8.6	$4>SOH + M^{2+} = (>SOH)_2 (>SO^-)_2\_ M^{2+} + 2H^+$	8.0	117.0	3.23	8.65	5.9	26.0
α-SiO$_2$[g]	Ca	0.4	$4>SOH + M^{2+} + H_2O = (>SOH)_2 (>SO^-)_2\_M(OH)^+ + 3H^+$	4.5	4.15	5.0	3.0	8.4	20.0
	Ca	−6.7	$4>SOH + M^{2+} + H_2O = (>SOH)_2 (>SO^-)^+\_M(OH)^+ + 3H^+$	4.5	4.15	5.0	3.0	8.4	26.9
	Ca	−13.7	$>SOH + M^{2+} + H_2O = >SO^-\_M(OH)^+ + 2H^+$	4.5	4.15	5.0	3.0	8.4	6.8
α-SiO$_2$[h]	Mg	−11.5	$>SOH + M^{2+} + H_2O = >SO^-\_M(OH)^+ + 2H^+$	11.4	4.2	17.7	1.2	8.4	7.6
	Mg	−0.5	$>SOH + M^{2+} = >SOH \ldots M^{2+}$	11.4	4.2	17.7	1.2	8.4	4.7
	Ca	−12.3	$>SOH + M^{2+} + H_2O = >SO^-\_M(OH)^+ + 2H^+$	11.4	4.2	17.7	1.2	8.4	6.8
	Ca	1.7	$>SOH + M^{2+} + H_2O = >SO^-\_M(OH)^+ + 2H^+$	11.4	4.2	17.7	1.2	8.4	7.7
am. SiO$_2$[i]	Ca	−8.8	$4>SOH + M^{2+} = (>SOH)_2 (>SO^-)_2\_M^{2+} + 2H^+$	4.6	388	10.0	2.8	8.4	19.2
	Ca	−15.1	$4>SOH + M^{2+} + H_2O = (>SOH)_2 (>SO^-)_2\_M(OH)^+ + 3H^+$	4.6	388	10.0	2.8	8.4	26.9
	Ca	−0.6	$>SOH + M^{2+} = >SOH \ldots M^{2+}$	4.6	388	10.0	2.8	8.4	7.7
am. SiO$_2$[j]	Mg	−5.3	$4>SOH + M^{2+} = (>SOH)_2 (>SO^-)_2\_M^{2+} + 2H^+$	4.6	131.2	3.0	2.8	8.4	19.3
	Mg	−0.5	$>SOH + M^{2+} = >SOH \ldots M^{2+}$	4.6	131.2	3.0	2.8	8.4	7.3

Values of $\log {}^*K_M^0$, refer to the reactions shown producing the surface species from $>SOH$ and H_2O, and were generated by regression of the data in Figs. 1–6 (see text) using the model parameters summarized in Table 1. Values of $\log K_M^\theta$ refer to the reactions producing the surface species from $> SO^-$ and OH^- and were calculated from the $\log {}^*K_M^0$ values with the aid of Eqs. (11)–(13) using the values of N_s, A_s, C_s, pH_{ZPC}, and ΔpK_n^θ given.

[a] Machesky et al. (1998).
[b] Jang and Fuerstenau (1986).
[c] Ali (1994).
[d] Balistrieri and Murray (1981).
[e] Hayes et al. (1987).
[f] Huang and Stumm (1973).
[g] Riese (1983).
[h] Vuceta (1976).
[i] Kosmulski (1994).
[j] Kent and Kastner (1985).

tetranuclear species was based on the X-ray standing wave studies discussed above. The state of protonation of this species and the choice of the mononuclear complex were based on the data depicted in Fig. 2 (see below). It can be seen in Fig. 1 that the calculated curves provide a close

description of the data within the uncertainties and approximations discussed.

The predicted model speciation of Ca on the surface of this rutile is also depicted in Fig. 1. It can be seen in the speciation plots that the relative proportions of tetra- and
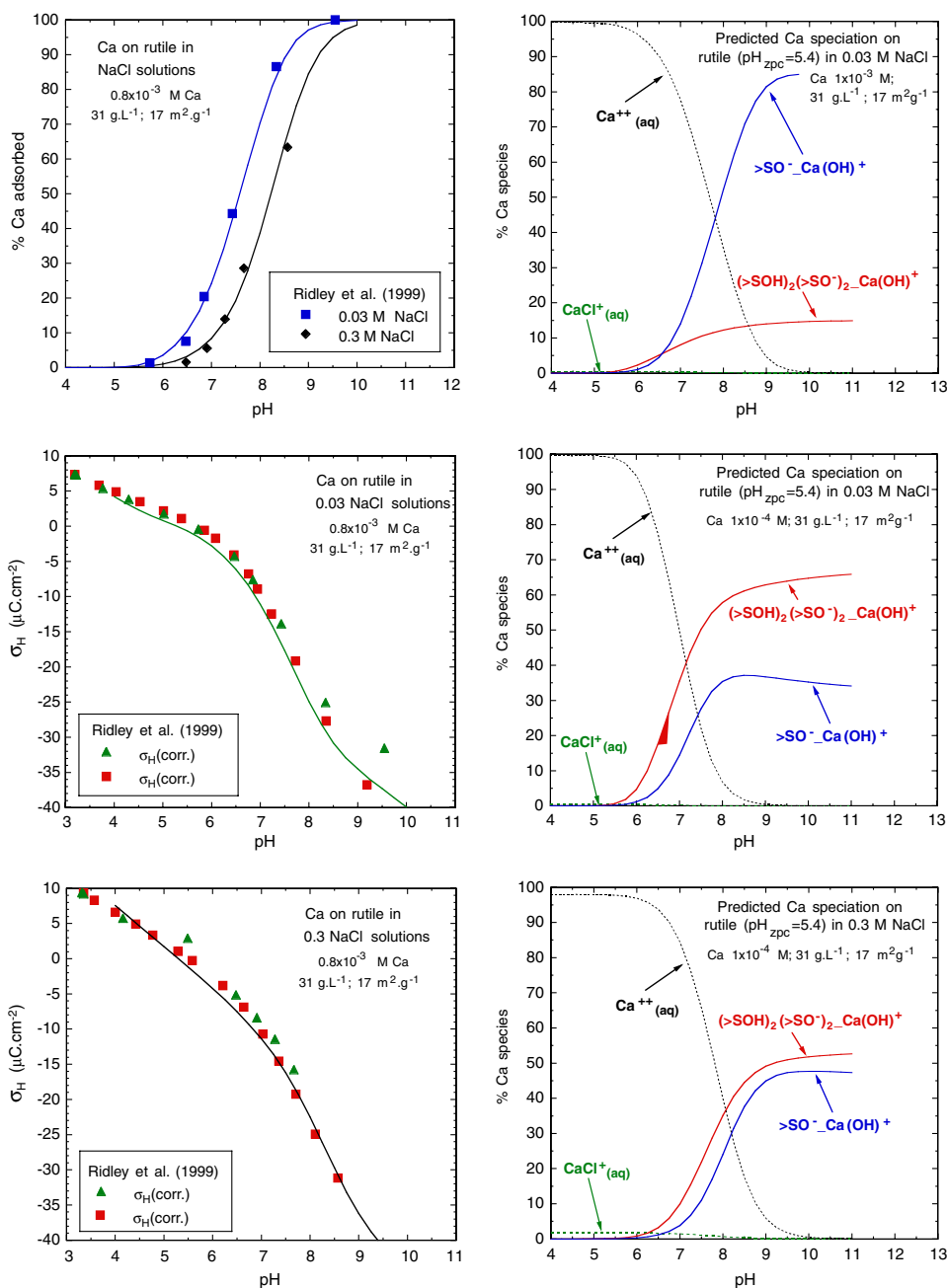
Fig. 1. Plots of Ca adsorption on rutile, proton surface charge, and predicted Ca speciation. The symbols represent experimental data. The curves in the left-hand panels represent regression of the data to obtain values of the equilibrium constants for the surface Ca species given in Table 2. The curves in the right-hand panels represent predicted abundances of aqueous and surface Ca species.

mono-species are a complex function of pH, ionic strength, and surface coverage. For total Ca concentrations $\geqslant 1 \times 10^{-3}$ M (surface coverage $\geqslant 1.9$ µmol m^{-2} at 100% adsorption of Ca), the mono-species is predicted to be dominant at pH values greater than about 6.5 U. However, for total Ca concentrations $\leqslant 1 \times 10^{-4}$ M, the tetra-species is dominant at $I \leqslant 0.03$ M, and the tetra- and mono-species are about equally abundant at $I = 0.3$ M.

The surface speciation results of the present study can be compared with the MUSIC model results for the same data sets published previously (Ridley et al., 2004). In the latter

study, the X-ray standing wave results for Sr adsorption on rutile were also used to pick tetranuclear coordination of the adsorbed Ca. It was found that a surface species represented as $(>TiOH^{-0.31})_2(>Ti_2O^{-0.62})_2\_Ca^{2+}$ placed on the 1 plane in between the 0 plane (for protons) and the 2 plane (for electrolyte adsorption) gave an adequate representation of the data. However, it was emphasized that other reaction stoichiometries (involving mono- and binuclear species) also fit the data equally well. In this model, two independent fitting parameters are involved, the equilibrium constant for the Ca adsorption and the capacitance
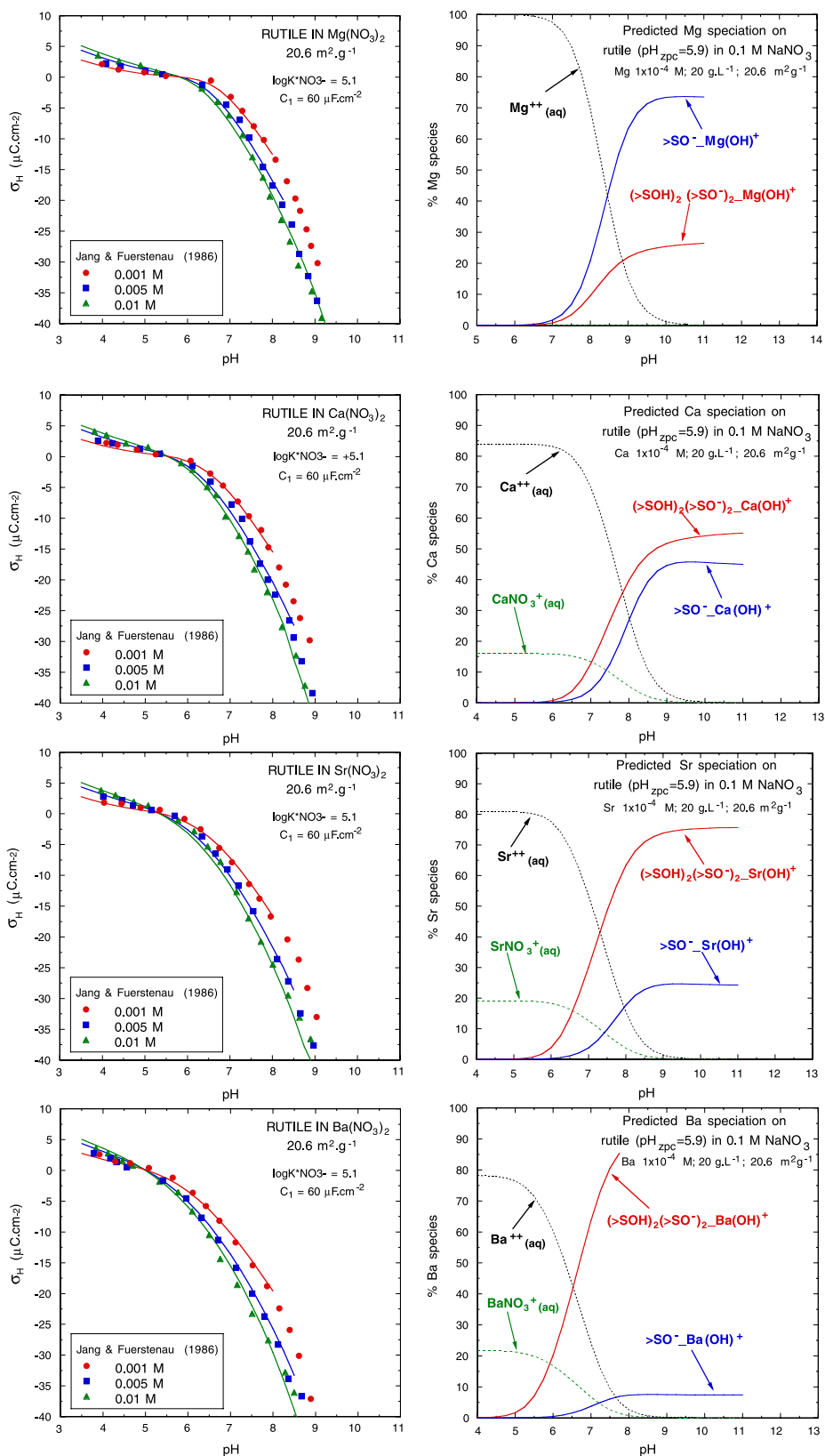
Fig. 2. Plots of proton surface charge for rutile in Mg, Ca, Sr, and Ba-nitrate solutions, and predicted alkaline earth speciation. The symbols represent experimental data. The curves in the left-hand panels represent regression of the data to obtain values of the equilibrium constants for the surface alkaline earth species given in Table 2. The curves are shown extending to the pH values at which the amount of metal adsorption significantly alters the ionic strength of the solution. The curves in the right-hand panels represent predicted abundances of aqueous and surface species in solutions with a constant ionic strength.

referring to the drop in potential between the 0 and 1 planes. Rather high values of the capacitance seem to be characteristic of such a model (e.g., 393 μF cm^{-2} for the tetranuclear species, and up to 613 μF cm^{-2} for a binuclear species). Such values can be rationalized, but only with dielectric constants approaching, or even exceeding that of bulk water. Furthermore, there is apparently no way to independently estimate these capacitances, or the equilibrium constants associated with them.

The fact that alternate reaction stoichiometries fit data such as those in Fig. 1 equally well has been repeatedly mentioned in the literature (Westall and Hohl, 1980; Sposito, 1986; Brown, 1990; Ridley et al., 2004). However, in all cases where this has been emphasized, the data being analyzed refer to a restricted range of conditions. For example, it can be seen in Fig. 1 that the data refer to a wide range of pH and ionic strength values, but only a single surface coverage value. It has been found in this study, and in previous studies (Criscenti and Sverjensky, 1999, 2002), that data over a wide range of surface coverages are essential in order to see a difference in the performance of surface complexation models with respect to tetranuclear vs. binuclear vs. mononuclear species. As an example, the data in Fig. 2 for proton surface charge on rutile in pure alkaline earth electrolyte solutions contain a surface coverage dependence that requires a combination of mononuclear and either binuclear or tetranuclear species, but not binuclear and tetranuclear. Consequently, the combination of analysis of adsorption data over wide ranges of all parameters and X-ray studies are essential to furthering our understanding of surface speciation.

The speciation used in the present study differs from the MUSIC model results discussed above because, two surface Ca species were used here, one tetranuclear and one mononuclear, both were Ca-OH complexes, and no additional capacitance parameter was used. It will be shown below that the same types of equilibrium constants are consistent with a very wide range of pH, ionic strength, surface coverages, and types of solid. In addition, these equilibrium constants vary systematically from one solid to another in ways that can be used to place them on a predictive basis.

2.2.2. Mg, Ca, Sr, and Ba on rutile from *Jang and Fuerstenau (1986)*

Experimental data for the proton surface charge on rutile in M(NO$_3$)$_2$ solutions (M = Mg, Ca, Sr or Ba) are represented by the symbols in Fig. 2. The adsorption of NO$_3^-$ on this sample of rutile was obtained from the data for proton surface charge in KNO$_3$ solutions shown in Fig. 3. Although the proton surface charge data shown in Fig. 2 were measured over a very wide range of pH values, the substantial uptake of M^{2+} at the two lowest ionic strengths resulted in decreasing ionic strengths approaching the highest pH values. Consequently, the solid regression curves depicted on the left-hand side of Fig. 2 were terminated at pH values where ionic strength changes of more than

about 10% took place. The model calculations incorporated the adsorption reactions producing (>SOH)$_2$(>SO$^-$)$_2$__M(OH)$^+$ and >SO$^-$_M(OH)$^+$ (Table 2).

The proton surface charge data in Fig. 2 proved relatively sensitive to the choice of model reactions. Assuming that the same reactions applied to all four alkaline earths, and that one of these involved a tetranuclear species (based on the Sr/rutile X-ray standing wave studies discussed above) enabled a definitive choice of two reactions. It was also discovered that all four datasets were consistent with a single value for the capacitance C$_1$ = 60 μF cm^{-2}. This capacitance is about 5–10 times lower than those obtained in the MUSIC model fits of Ca-adsorption on rutile (Ridley et al., 2004) discussed above. The value of 60 μF cm^{-2} is, however, consistent with the low dielectric constants to be expected close to the rutile surface. It can be seen in Fig. 2 that the calculated curves provide a close description of the data within the uncertainties and approximations discussed. Furthermore, it can be seen in Fig. 3 that prediction of the amount of metal adsorbed agrees closely with the experimental data shown in the figure. Again, because the comparison is made at 0.001 M, the calculations are limited to a maximum pH = 8.0.

It can also be seen in Fig. 3 that the predicted zeta potentials are in qualitative agreement with the experimental data. It should be noted that the uncertainties in the zeta potential data are substantial, but difficult to estimate. For instance, the zeta potentials for rutile in KNO$_3$ reported by Jang and Fuerstenau (1986) lie at more positive values than those previously reported for the same solid and electrolyte (Wiese and Healy, 1975). This may account, at least in part, for the discrepancies between calculated and measured zeta potentials in Fig. 3 at pH ⩽ 6, where adsorption of M^{2+} is neligable. At higher pH values, where progressive adsorption of M^{2+} takes place, the model predicts the most important feature of the zeta potentials, namely the reversal of surface charge leading to increasingly positive values. With the triple-layer model, this type of behavior is only caused by the adsorption reaction producing >SO$^-$_M(OH)$^+$ (first demonstrated for Cd/rutile by James et al., 1981).

The predicted model speciation of Mg, Ca, Sr, and Ba on the surface of this rutile is depicted in Fig. 2. It can be seen in the speciation plots that there is a systematic shift from dominantly mono-species to tetra-species in the sequence Mg, Ca, Sr, Ba. The Mg speciation is dominated by the mono-species, the large ions Sr and Ba are dominated by the tetra-species, and the intermediate-size Ca is a mix, depending on the conditions as noted above in Fig. 1. This result is broadly consistent with the X-ray standing wave results for Sr which have reported the tetra-species only. It can be seen in Fig. 2 that under at least some conditions the predicted amount of mono-species for Sr may be sufficiently small that it would be difficult to detect experimentally. It is also interesting to note that molecular dynamics calculations (Predota et al., 2004a,b; Zhang et al., 2004a,b) show evidence of two species of Ca on a
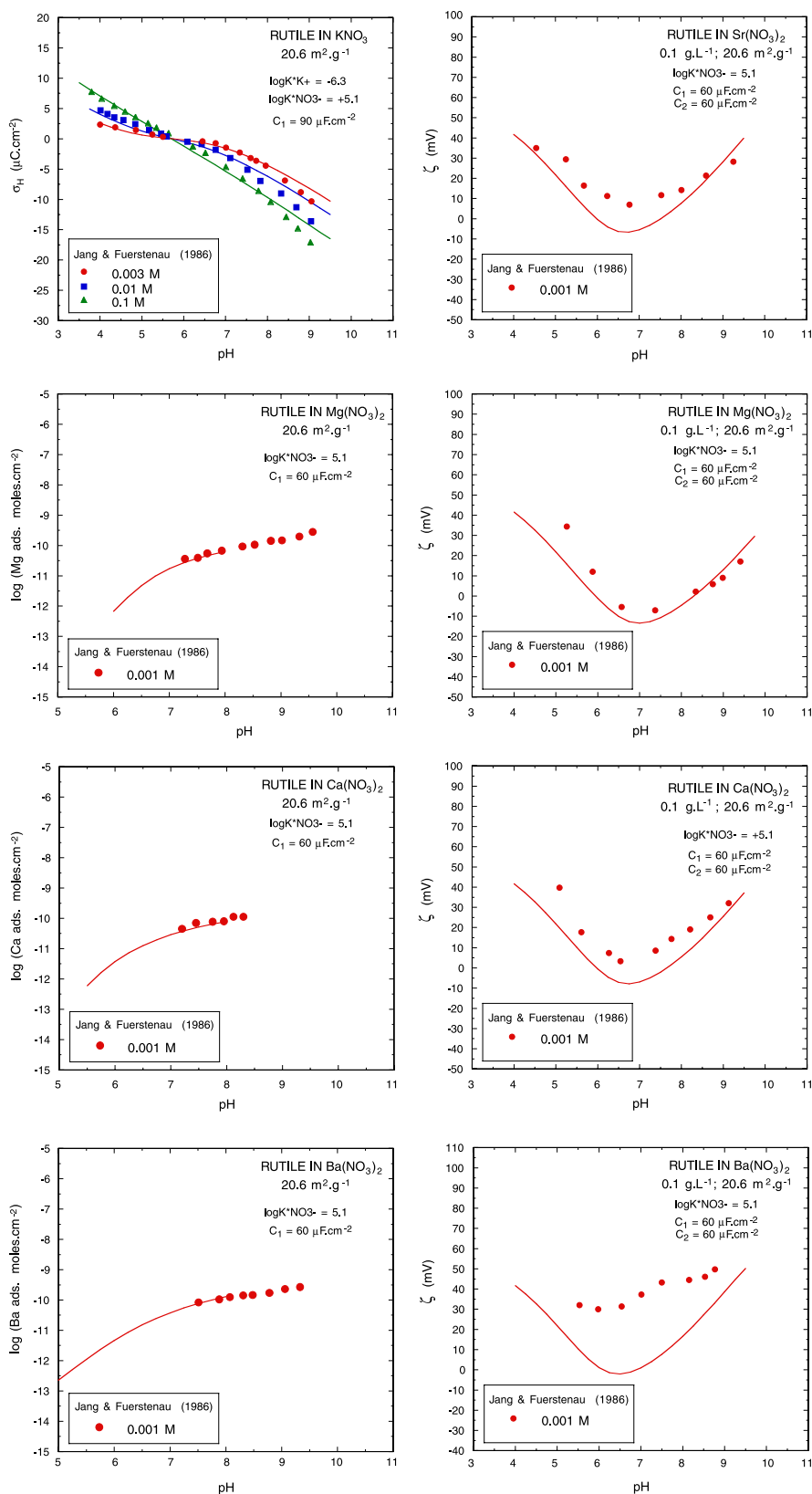
Fig. 3. Plots of proton surface charge on rutile in KNO$_3$ solutions, and plots of alkaline earth adsorption and ζ-potentials on rutile in alkaline earth nitrate solutions. The symbols represent experimental data. The proton surface charge curves represent regression of the data. However, the other solid curves represent independent prediction of adsorption and the ζ-potential based on the regression curves shown in Fig. 2. The predicted adsorption curves are shown extending to the pH values at which the amount of metal adsorption significantly alters the ionic strength of the solution.

hydroxylated rutile surface, but only one for Sr, which again is in qualitative agreement with the predicted speciation in Fig. 2.

2.3. Mg and Ca on goethite

2.3.1. Ca on goethite from Ali and Dzombak (1996)

Experimental data for the adsorption of Ca on goethite in NaCl solutions are represented by the symbols in Fig. 4. Uncertainties in the experimental values for % Ca adsorbed

are cited as ± 4 (Ali and Dzombak, 1996). It can be seen in Fig. 4 that most of the data refer to 0.01 M NaCl over a wide range of total Ca concentrations from 0.001 to 0.25 mM (i.e., surface coverages at 100% Ca adsorption of 0.008–2.0 µmols m^{-2}). The four solid curves depicted on the left-hand side of Fig. 4 represent calculations using the adsorption reactions producing $(>SOH)_2(>SO^-)_2\_Ca^{2+}$, $(>SOH)_2(>SO^-)_2\_Ca(OH)^+$ and $>SO^-\_Ca(OH)^+$ (Table 2). The data at the lowest surface coverages in Fig. 4 required the reaction producing the tetranuclear species $(>SOH)_2$
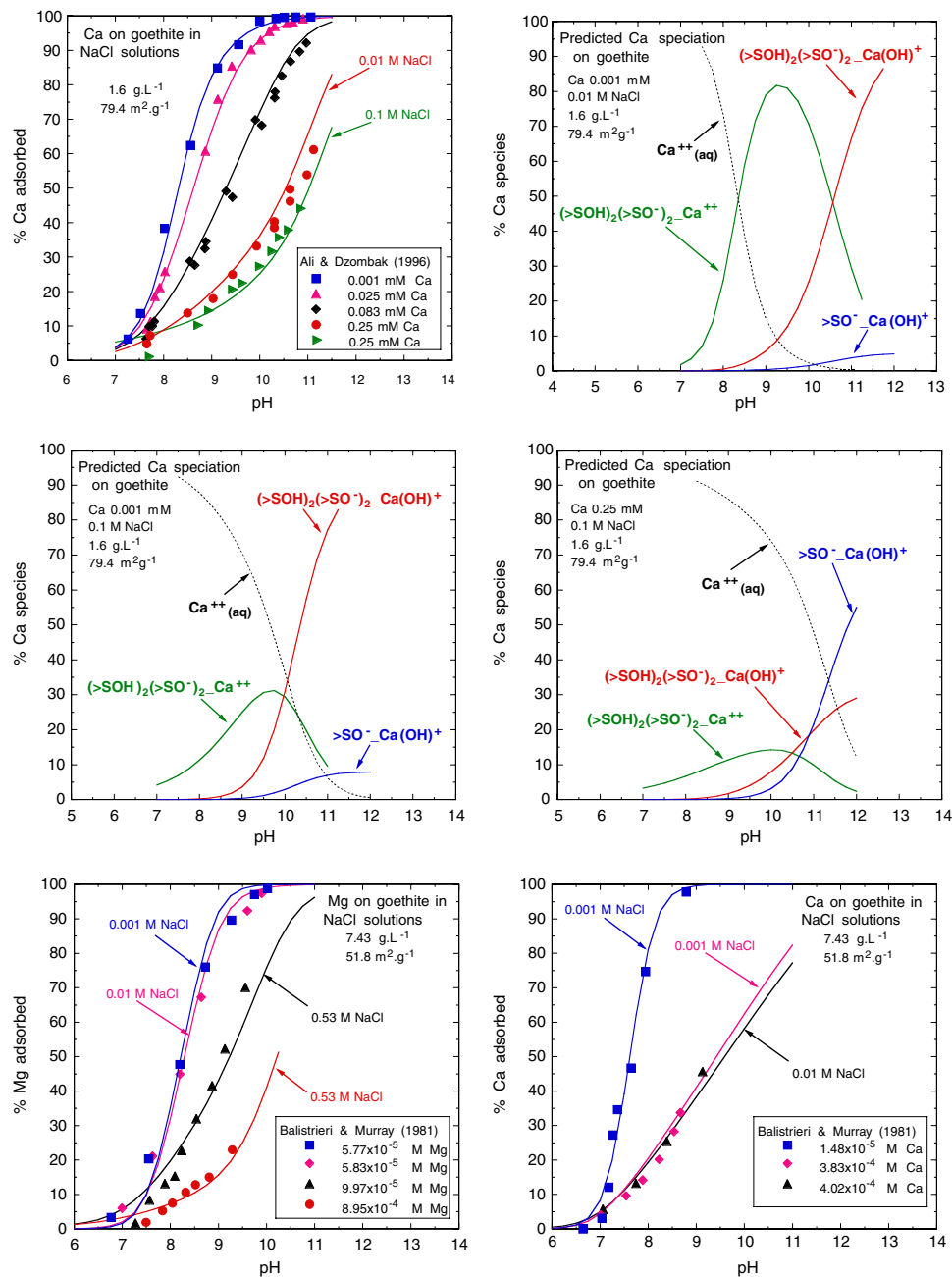

Fig. 4. Plots of Ca and Mg adsorption on two different goethites and the predicted Ca speciation. The symbols represent experimental data. The curves in figures containing data represent regression of the data to obtain values of the equilibrium constants for the surface Ca and Mg species given in Table 2. It can be seen in the predicted Ca-speciation plots that the proportions of surface Ca species vary strongly as a function of pH, ionic strength, and surface coverage.

($>SO^-$)$_2$_Ca^{2+} or a binuclear equivalent. The tetranuclear species was chosen based on the assumptions discussed above. Selection of the protonated version of this species and the mononuclear complex were based on regression of the data at higher surface coverages and at higher ionic strengths. It can be seen in Fig. 4 that the calculated curves provide a close description of the data within the uncertainties and approximations discussed.

The predicted model speciation of Ca on goethite is also depicted in Fig. 4. It can be seen that the speciation is a complex function of pH, ionic strength, and surface coverage. For all Ca concentrations depicted (i.e., surface coverages 0.008–2.0 µmol m^{-2} at 100% adsorption) and pH $\leqslant$ 10, the two tetra-species predominate over the mono-species. Under these conditions, the unhydrolyzed tetra-species is more important than the hydrolyzed species at I $\leqslant$ 0.01 M. The reverse is true at higher ionic strengths. However, at Ca concentrations $\geqslant$ 0.25 mM, the mono-species predominates at pH $\geqslant$ 11.

2.3.2. Mg and Ca on goethite from Balistrieri and Murray (1981)

Experimental data for the adsorption of Mg and Ca on goethite inNaCl solutions are represented by the symbols in Fig. 4. It should be noted that the pH$_{PZSE}$ of this goethite is only 7.6, which suggests that it contains significant amounts of carbonate. Relative to the data for Ca on goethite discussed above, it can be seen in the figure that the experimental data from Balistrieri and Murray (1981) correspond to a more limited range of surface coverages (e.g., 0.15 to 2.3 µmol m^{-2} at 100% Mg adsorption), but a much wider range of ionic strengths in the case of Mg. For both Mg and Ca, the data at low ionic strengths, 0.001 and 0.01 M NaCl, only required the reaction producing the species ($>SOH$)$_2$($>SO^-$)$_2$_M^{2+}—the same reaction determined by the data from Ali and Dzombak (1996) discussed above. In the case of Mg at 0.53 M NaCl, the two model curves also include the adsorption reactions producing $>SO^-$_$Mg(OH)^+$ and ($>SOH$)$_2$($>SO^-$)$_2$_$Mg(OH)Cl$ (Table 2). The latter species were required by these data referring to high ionic strengths.

2.4. Ca on amorphous silica and quartz

2.4.1. Ca on amorphous silica from Kosmulski (1994)

Experimental data for the adsorption of Ca on silica in NaCl solutions are represented by the symbols in Fig. 5. It can be seen that the data refer to a single low surface coverage (0.0026 µmol m^{-2} at 100% Ca adsorption), but a wide range of pH values and ionic strengths at two temperatures (15 and 35 °C). The three solid curves depicted on the left-hand side of Fig. 5 represent calculations referring to 25 °C using the adsorption reactions producing ($>SOH$)$_2$($>SO^-$)$_2$_Ca^{2+}, ($>SOH$)$_2$($>SO^-$)$_2$_ $Ca(OH)^+$, and $>SOH...Ca^{2+}$ (Table 2). The tetranuclear species were chosen based on the assumptions discussed above. As in the case of goethite, both protonated and non-protonated

versions of tetranuclear species were needed, based on regression of the data at the two higher ionic strengths. The data at the lowest ionic strength required the reaction producing the d-plane species $>SOH...Ca^{2+}$. A similar species was used for Cu adsorption onto quartz at low ionic strengths (Criscenti and Sverjensky, 1999) and may correspond to an outer-sphere Cu-complex on quartz detected spectroscopically (Hyun et al., 2003). A d-plane species was also found necessary for Mg on silica and Ca on quartz (see below). It becomes completely unimportant at higher ionic strengths. It can be seen in Fig. 5 that the calculated curves provide a reasonable description of the data within the ranges given by the different temperatures.

The predicted model speciation of Ca on silica in NaCl solutions is also depicted in Fig. 5. It can be seen at I $\leqslant$ 0.01 M, that the adsorption of Ca is dominated by the d-plane complex at pH $\leqslant$ 8. At higher pH values the tetra-species predominate. At the highest ionic strength, the hydrolyzed tetra-species is responsible for most of the Ca-adsorption.

2.4.2. Ca on quartz from Riese (1983)

Experimental data for the proton surface charge of quartz in CaCl$_2$ solutions are represented by the symbols in Fig. 5. It can be seen in Fig. 5 that the data like the silica discussed above refer to a wide range of pH and ionic strengths. The major difference is the much higher surface coverage ($\geqslant$ 40 µmol m^{-2} if it were possible to have 100% Ca adsorption). Given that surface speciation can be a strong function of surface coverage, it is perhaps not surprizing that the adsorption reactions discovered for Ca on quartz differ in some respects to the ones described above for amorphous silica. The three solid curves represent calculations for adsorption on quartz using the reactions producing ($>SOH$)$_2$($>SO^-$)$_2$_Ca^{2+}, ($>SOH$)$_2$ ($>SO^-$)$_2$ _$Ca(OH)^+$, and $>SO^-$_$Ca(OH)^+$ (Table 2). The predicted speciation in 0.1 MNaCl solutions is also given in Fig. 5 for comparison with the results for silica. Two differences between the speciation of Ca on quartz and amorphous silica can be seen in the figure. The reaction producing $>SO^-$_$Ca(OH)^+$ on quartz is characteristic of high surface coverage data. The absence of the d-plane complex on quartz, and its importance on amorphous silica, may simply be a consequence of the relative insensitivity of surface protonation data to such a complex.

2.5. Summary of types of adsorption reactions

The complete range of experimental data depicted in Figs. 1–5 indicates that a quantitative description of alkaline earth adsorption on rutile, goethite, quartz, and amorphous silica requires five different reaction stoichiometries (Table 2). Three of these are tetranuclear and two are mononuclear reactions. It should be emphasized that this is a model result: only the tetranuclear species on rutile are based on X-ray evidence. The rest have been inferred from adsorption data covering wide ranges of conditions
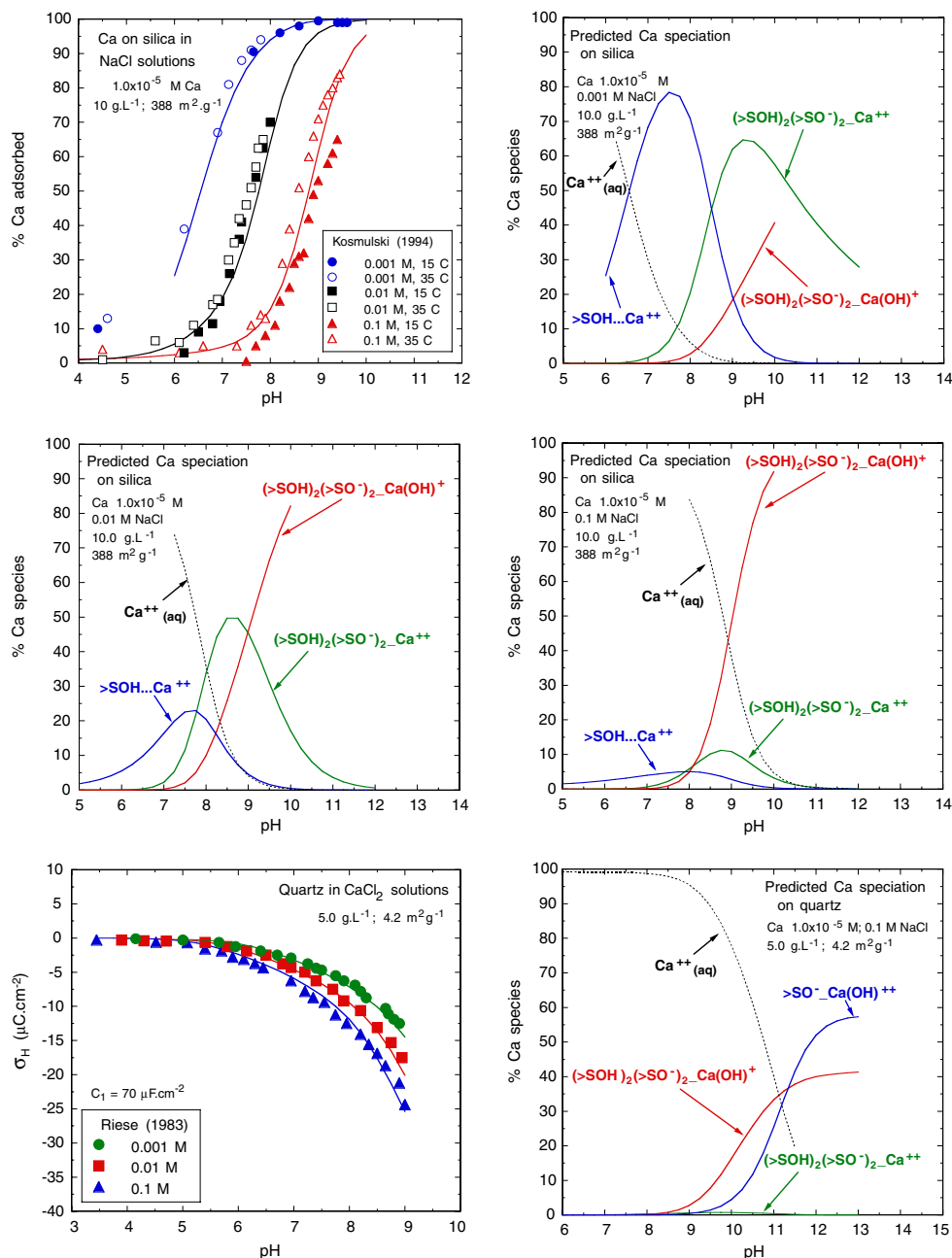
Fig. 5. Plots of Ca adsorption on amorphous silica and the proton surface charge associated with Ca adsorption on quartz, as well as predicted Ca-surface speciation on the silica and quartz. The symbols represent experimental data. The curves in figures containing data represent regression of the data to obtain values of the equilibrium constants for the surface Ca species given in Table 2.

and remain to be tested by X-ray and spectroscopic measurements. In the meantime, it is interesting to note that several of the inferred reactions are common to a number of alkaline earths and minerals. In addition, the need for different reactions varies systematically according to the cation of interest, the mineral, and the solution chemistry. This suggests that it is possible to predict the type of adsorption reactions both qualitatively and quantitatively, which is a major goal of the current study.

It can be seen in Table 2 that the two reactions producing $(>SOH)_2(>SO^-)_2\_Ca(OH)^+$ and $>SO^-\_Ca(OH)^+$ are common to rutile, goethite, and quartz. Features such as

this will provide the basis for correlations and quantitative prediction of equilibrium adsorption constants (see below). Qualitative inference of the types of adsorption reactions can also be made from systematic variations in Table 2. Variations according to the cation of interest were noted above for rutile (Fig. 2). Systematic variations with the type of mineral are also evident in Figs. 1–5. For example, the *d*-plane complex has been inferred for both Mg and Ca adsorption on silica (Table 2). Finally, systematic variations with solution chemistry occur. For example, at very high ionic strengths on goethite a mixed tetranuclear-OH-Cl complex has been inferred (Table 2).

The systematic variations noted above serve as a useful guide to the selection of adsorption reactions where a limited range of experimental data is available. Additional data for the adsorption of alkaline earths referring to limited ranges of pH, ionic strength, and surface coverage are given in Fig. 6. These data serve as a test of the applicability of the range of different types of surface species described above. In addition, the application of the adsorption reactions described above to the data in Fig. 6 enables characterization of additional equilibrium constants that facilitate the development of theoretical predictive relationships.

2.6. Expected adsorption reactions tested with additional data for goethite, quartz, and silica

It can be seen in Fig. 6 and Table 2 that the adsorption of Mg and Ca on quartz at low ionic strengths can be well described by a combination of two species expected from the adsorption and speciation plots for quartz and silica in Fig. 5 At pH values of 5 to 8, the species $>SOH{\ldots}M^{2+}$ predominates, and at higher pH values the species $>SO^-\_M(OH)^+$ predominates. Similarly, the curves describing adsorption of Mg on silica in Fig. 6 refer to the species $(>SOH)_2(>SO^-)_2\_Mg^{2+}$ and $>SOH{\ldots}Mg^{2+}$.

A more complex set of species is required to describe the adsorption of Ba on goethite (Fig. 6, Table 2). For a large alkaline earth such as Ba, tetranuclear complexes are expected, based on the trends with cation size discussed above for rutile. At the lower ionic strengths in Fig. 6 (0.002 and 0.1 M), the tetranuclear species $(>SOH)_2(>SO^-)_2\_Ba(OH)^+$ was found to contribute significantly, but only at pH values above about 8. At the lower pH values of about 6 to 8, where the Ba adsorbs strongly against a positively charged surface, a different tetranuclear complex was found necessary: $(>SOH)_4\_Ba(OH)^+$. This type of species, where the Ba adsorbs to neutral sites instead of negative sites, is consistent with the expected low abundance of negative sites at pH = 6 to 8. At the highest ionic strengths (1.0 M), and pH values above about 8, the mixed tetranuclear electrolyte Ba-hydroxide complex, $(>SOH)_2(>SO^-)_2\_Ba(OH)NO_3$, analogous to that described above for Mg on goethite at high ionic strengths, was found to be essential to describe the data. It is interesting that all three species for Ba adsorption on goethite are tetranuclear as expected from the rutile model speciation. However, this conclusion should be tested with X-ray experiments.

Trends of speciation with pH and alkaline earth cation radius were also found in analyzing the surface protonation data associated with Mg, Ca, Sr, and Ba adsorption on γ-alumina depicted in Fig. 6. For example, it can be seen in Fig. 6 that the amount of proton release at pH = 10 decreases in the sequence Mg > Ca > Sr > Ba, indicating that the strength of adsorption of the alkaline earths decreases in the same way. This trend is opposite to that noted above for the strength of alkaline earth adsorption on rutile. Analysis of the surface protonation data in

Fig. 6 revealed that at pH values of 6.0 to about 8.5, the tetranuclear species $(>SOH)_2(>SO^-)_2\_M^{2+}$ predominates, followed at 8.5 to about 10.0 by the tetranuclear species $(>SOH)_2(>SO^-)_2\_M(OH)^+$, followed at pH > 10.0 by the mononuclear species $>SO^-\_M(OH)^+$. In the case of Ba, however, the mononuclear species was not detected. Again, this is consistent with the results cited above for Ba adsorption on rutile and goethite.

3. Application of solvation and crystal–chemical theory

3.1. Correlations of equilibrium constants with dielectric constant and Pauling bond strength

The standard Gibbs free energy of the vth cation adsorption reaction ($\Delta G_{r,v}^\theta$, site-occupancy standard states, Appendix A) is broken into three terms according to

$$\Delta G_{r,v}^\theta = \Delta G_{s,v}^\theta + \Delta G_{ai,v}^\theta + \Delta G_{ii,v}^\theta, \tag{9}$$

where $\Delta G_{s,v}^\theta$ represents a Born solvation contribution, $\Delta G_{ai,v}^\theta$ represents an electrostatic interaction between the absorbate and near-surface species, and $\Delta G_{ii,v}^\theta$ represents a term intrinsic to the aqueous adsorbate. The Born solvation term is treated here by building on earlier studies of metal and electrolyte cation and anion adsorption. The electrostatic interaction term for a cation is obtained by summing an attractive interaction between the cation and a surface oxygen with a repulsive interaction between the cation and the underlying metal of the solid sorbent.

Assuming that the solvation contribution depends primarily on the inverse of the dielectric constant of the solid (ε_s) as described previously (Sahai and Sverjensky, 1997b; Sverjensky, 2005; Sverjensky and Sahai, 1996) and that the electrostatic interaction terms depend primarily on the repulsive interactions described above results in the following general equation for the logarithm of the equilibrium constant for metal adsorption:

$$\log K_M^\theta = \frac{-\Delta\Omega_{r,M}}{2.303RT}\left(\frac{1}{\varepsilon_s}\right) - B_M\left(\frac{s}{r_M}\right) + \log K_{ii,M}''. \tag{10}$$

In Eq. (10), the first term on the right-hand side represents the solvation term in Eq. (9) and $\Delta\Omega_{r,M}$ represents a Born solvation coefficient for the rth reaction containing the metal M^{2+}. The second term represents the repulsive interactions of the electrostatic term in Eq. (9). In this term, s represents the Pauling bond strength (Sverjensky and Sahai, 1996) and r_M the distance over which the adsorbing ion M^{2+} is repulsed by the underlying cation of the solid. The third term represents not only the intrinsic interactions in Eq. (9), it also includes solvation contributions involving the interfacial dielectric constant and the electrostatic attractive interactions, all of which are approximated here to be constants for a given adsorbate.

Values of the logarithms of metal adsorption equilibrium constants for site-occupancy standard states ($\log K_M^\theta$) for use in Eq. (10) were calculated from the values referring to the hypothetical 1.0 M standard state ($\log {}^*K_M^0$) obtained
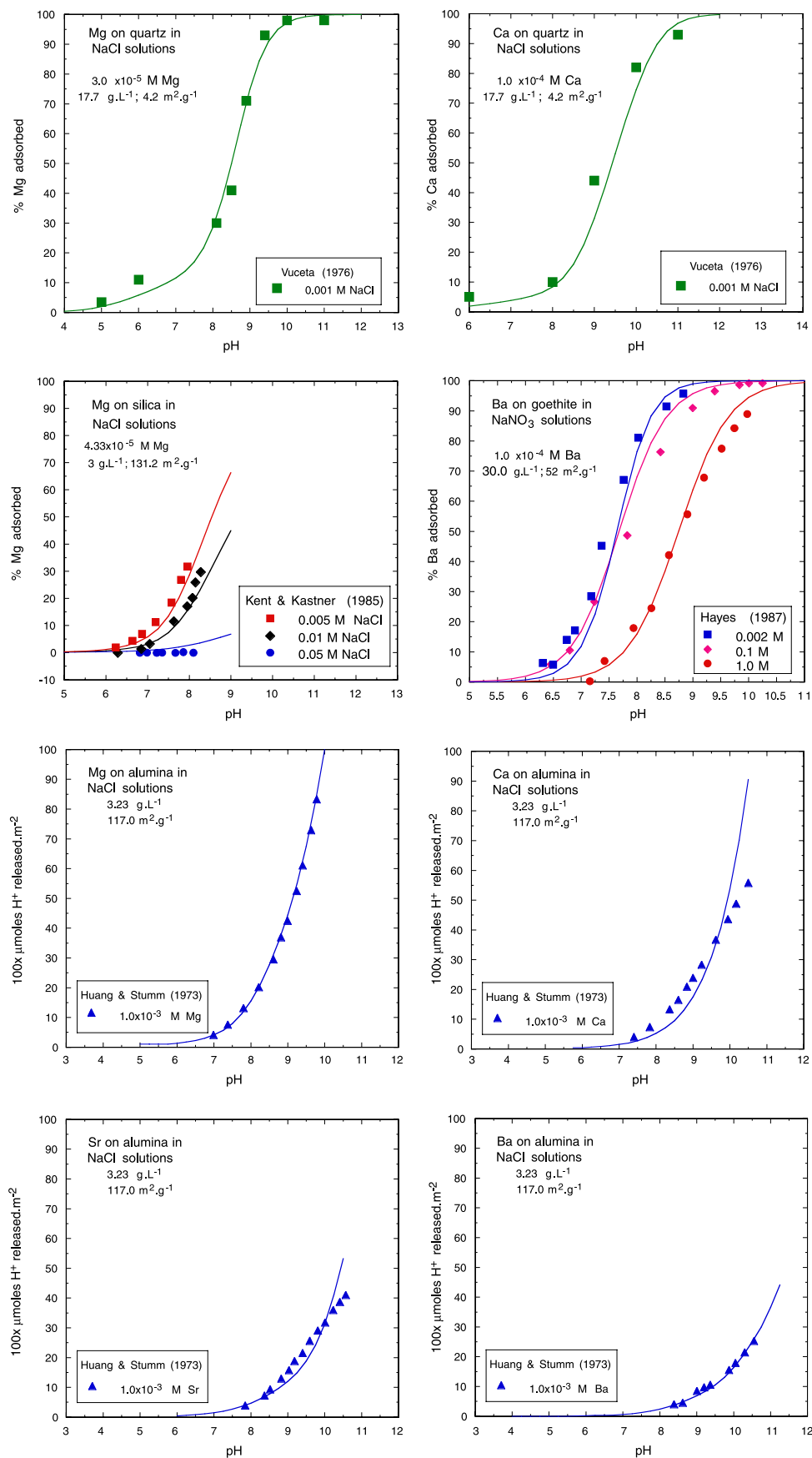
Fig. 6. Plots of Mg, Ca, Sr, and Ba adsorption on quartz, silica, goethite, and alumina. The symbols represent experimental data. The solid curves represent regression of the data to obtain values of the equilibrium constants for the surface species given in Table 2.

by regression of the experimental data described above (Table 2) with equations from the Appendix A:

$$\log K^{\theta}_{>SO^- \_M(OH)^+} = \log {}^*K^0_{>SO^- \_M(OH)^+} + pH_{ZPC}$$
$$+ \frac{\Delta pK^{\theta}_n}{2} + \log\left(\frac{N_s A_s}{N^{\ddagger}A^{\ddagger}}\right) + 14.0, \quad (11)$$

$$\log K^{\theta}_{tet.M(OH)^+} = \log {}^*K^0_{tet.M(OH)^+} + 2pH_{ZPC} + \Delta pK^{\theta}_n$$
$$+ \log\left(\frac{(N_s A_s)^4}{(N^{\ddagger}A^{\ddagger})^2} C_s^3\right) + 14.0, \quad (12)$$

$$\log K^{\theta}_{tet.M^{2+}} = \log {}^*K^0_{tet.M^{2+}} + 2pH_{ZPC} + \Delta pK^{\theta}_n$$
$$+ \log\left(\frac{(N_s A_s)^4}{(N^{\ddagger}A^{\ddagger})^2} C_s^3\right). \quad (13)$$

The values of $\log K^{\theta}_M$ are given in Table 2. The corresponding equilibria are listed in Table 3. It should be noted that Eqs. (11)–(13) correct the equilibrium constants for differences in pH_{ZPC} and ΔpK, as well as differences in sample properties

such as surface area and site density according to the standard states defined in Appendix A. In addition, the reactions involving formation of a metal hydroxide surface species have been modified by the addition of $\log K_{H_2O}$ (=14.0) to express hydroxyl added to the left-hand side of the reaction. The resulting equilibrium constants $\log K^{\theta}_M$ were used in the regression calculations described below (Fig. 7). Only those values from Table 2 where more than one value for a given metal and reaction were available were included in Fig. 7. In several cases, only two values were available to plot in Fig. 7. It was assumed in these plots that a linear relationship existed analogous to the plots containing more values. Uncertainties in $\log K^{\theta}_M$ are estimated to be about ± 0.3 based on an estimation of the uncertainties in $\log {}^*K^0_M$. These uncertainties are depicted as error bars on the points plotted in Fig. 7.

Regression of the values of $\log K^{\theta}_M$ from Table 2 with Eq. (10) in terms of the parameters $\frac{1}{\varepsilon_s}$ and $\frac{s}{r_M}$ (Sverjensky, 2005) resulted in the lines of best fit shown in Fig. 7, and the slopes and intercepts given in Table 3. For the reactions

Table 3
Regression slopes and intercepts from Fig. 7 used to generate the values of $\Delta\Omega_{r,M}$ and $\log K''_{ii,M}$, depicted in Figs. 8 and 9 (respectively)

Ion	Slopes	Intcpts. ($\log K''_{ii,m}$)	$\Delta\Omega_{r,M}$[a]expt.	$r_{hydr.,M}$[b]	γ_j[c]	$\Omega^{abs,}_{int.,j}$[c]	$\Delta\Omega_{r,j}$ pred.	Slopes pred.	$r_{x,M}$[d]	$\log K''_{ii,M}$ pred.
$>SO^- + M^{2+} + OH^- = \ >SO^-\_M(OH)^+$										
Be^{2+}				4.08	−0.55	35.19	11.84	−8.68	0.45	10.81
Mg^{2+}	−16.01	11.24	21.84	3.46	−0.55	35.19	21.86	−16.03	0.72	11.21
Ca^{2+}	−22.10	11.61	30.15	3.09	−0.55	35.19	30.17	−22.12	1.00	11.62
Sr^{2+}	−25.80	11.77	35.20	2.91[f]	−0.55	35.19	35.16	−25.77	1.16	11.86
Ba^{2+}		12.22[e]		2.70[g]	−0.55	35.19	42.03	−30.81	1.36	12.16
Ra^{2+}				2.60[h]	−0.55	35.19	45.80	−33.57	1.39	12.20
$2 >SOH + 2 >SO + M^{2+} + OH^- = (>SOH)_2>SO^-)_2 \_M(OH)^+$										
Be^{2+}				4.08	−1.586	78.05	0	0.0	0.45	29.38
Mg^{2+}		31.01[e]		3.46	−1.586	78.05	10.5	−7.73	0.72	31.00
Ca^{2+}	−23.69	32.71	32.33	3.09	−1.586	78.05	32.3	−23.71	1.00	32.67
Sr^{2+}	−34.71	33.54	47.34	2.91[f]	−1.586	78.05	47.3	−34.71	1.16	33.63
Ba^{2+}	−52.00	34.88	70.94	2.70[g]	−1.586	78.05	71.0	−52.03	1.36	34.83
Ra^{2+}				2.60[h]	−1.586	78.05	85.7	−62.81	1.39	35.01
$2>SOH + 2>SO^- + M^{2+} = (>SOH)_2 (>SO^-)_2\_M^{2+}$										
Be^{2+}				4.08	−1.586	78.05	0.0	0.0	0.45	27.27
Mg^{2+}	−7.73[i]	28.47[j]		3.46	−1.586	78.05	10.5	−7.73	0.72	28.47
Ca^{2+}	−23.71[i]	29.71[j]		3.09	−1.586	78.05	32.3	−23.71	1.00	29.71
Sr^{2+}				2.91[f]	−1.586	78.05	47.3	−34.71	1.16	30.42
Ba^{2+}				2.70[g]	−1.586	78.05	71.0	−52.03	1.36	31.30
Ra^{2+}				2.60[h]	−1.586	78.05	85.7	−62.81	1.39	31.44

The correlations in the latter figures and Eqs. (20)–(24) together with the values of the parameters $r_{hydr.,M}$, γ_j $\Omega^{abs.}_{int.,j}$ and $r_{x,M}$, listed were used to predict slopes and $\log K''_{ii,M}$, values for all the alkaline earths.

[a] Calculated from the given slopes and the first term on the right hand side of Eq. (10).

[b] Hydrated radii (Å) from Robinson and Stokes (1959; p. 126) unless otherwise stated.

[c] Regression coefficients in Eq. 21 and Fig. 8 (Å and cal mol^{-1} K^{-1}, respectively).

[d] Crystallographic VI-fold radii (Å) from Shannon and Prewitt (1969).

[e] Calculated from $\log K^{\theta}_M$ rutile given in Table 2 and the predicted slopes listed above.

[f] Hydrated radius estimated from the slope for $>SO^-\_Sr(OH)^+$ and the systematics defined by $>SO^-\_Mg(OH)^+$ and $>SO^-\_Ca(OH)^+$ in Fig. 8.

[g] Hydrated radius estimated from the slope for $(>SOH)_2 (>SO^-)_2\_Ba(OH)^+$ and the systematics defined by $(>SOH)_2 (>SO^-)_2\_Ca(OH)^+$ and $(>SOH)_2$ $(>SO^-)_2\_Sr(OH)^+$ in Fig. 8.

[h] Hydrated radius estimated from a non-linear regression of hydrated vs. crystallographic radii.

[i] Assumed equal to the values predicted for $\log K^{\theta}_{tet.M(OH)^+}$ for Mg and Ca.

[j] Obtained by regression of the $\log K^{\theta}_M$ values for Mg and Ca using Eq. 10 with predicted slopes and $B_M = 53.61$ and 25.57, respectively. Values of B_M were also obtained for Sr and Ba by regression of $\log K^{\theta}_M$ values given in Table 2 using Eq. 10 with the predicted slopes and intercepts given above, resulting in $B_M = 9.0$ and 4.0, respectively. Based on these values of B_M for Mg, Ca, Sr, and Ba, a correlation with radius was used to estimate values of B_M for Be and Ra equal to 133 and 2, respectively.
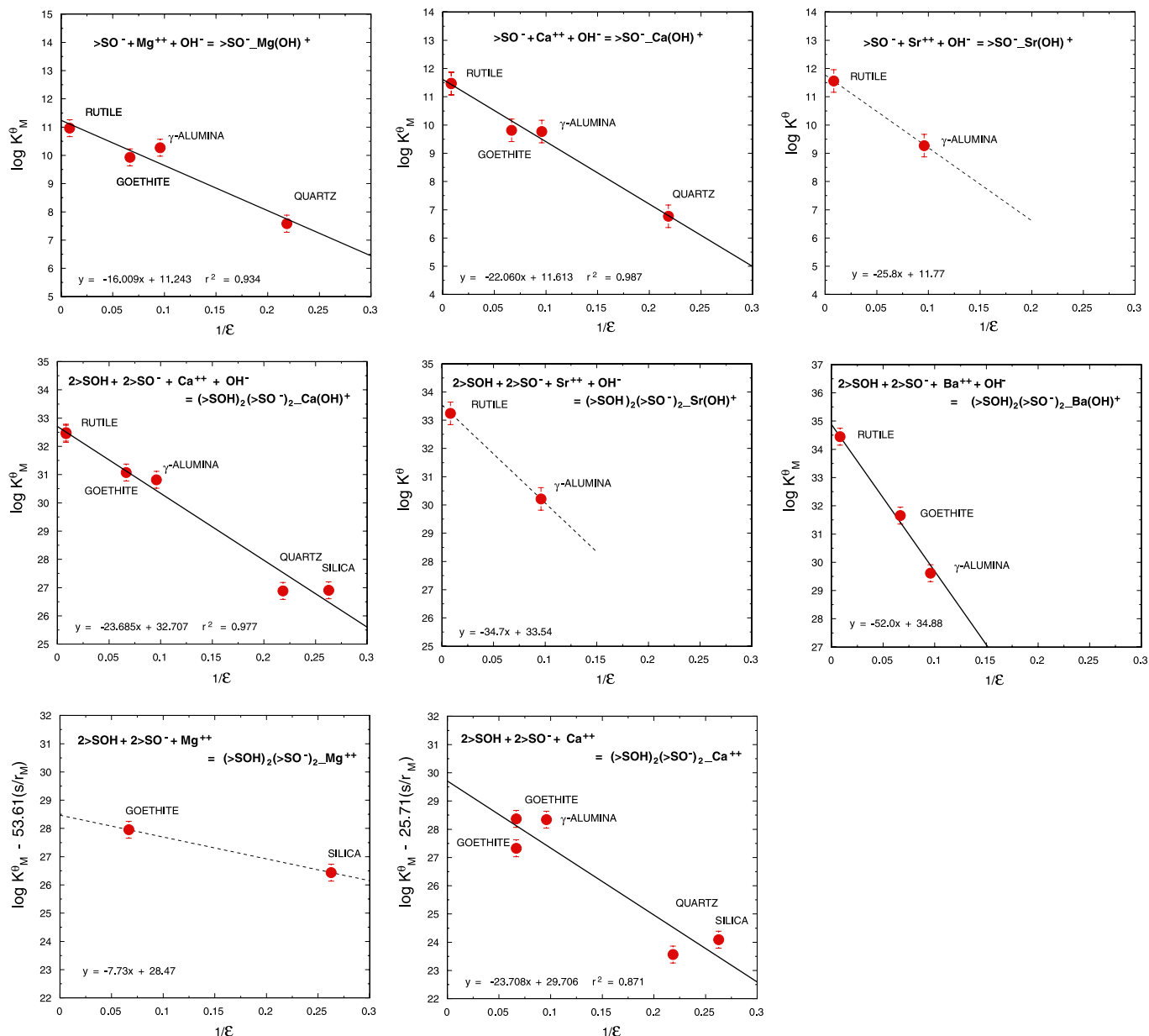
Fig. 7. Equilibrium constants for alkaline earth adsorption for three different reaction stoichiometries plotted as a function of the inverse of the dielectric constant of the solid. The symbols represent values of $\log K^0$ from Table 2 referring to internally consistent standard states, corrected for differences in site density, surface area, solid concentration, pH_{ZPC}, and ΔpK_n^θ (Table 2). The solid and dashed lines represent regression of the data resulting in the slopes and intercepts listed in Table 3.

resulting in the adsorption of a hydroxide complex, no repulsion term involving $\frac{s}{r_M}$ was necessary (i.e., the data are consistent with $B_M = 0$ in Eq. 10). This suggests that a monovalent $M(OH)^+$ species on the surface is shielded from electrostatic interaction with the underlying metal belonging to the bulk crystal structure. If true, it would be expected that for an adsorbed divalent cation M^{2+} the +2 charge on the cation could be associated with a significant electrostatic repulsion by underlying metals. Consistent with this suggestion, a value of $B_M = 25.71$ was found necessary for the reaction producing $(>SOH)_2$ $(>SO^-)_2$_Ca^{2+} in Fig. 7. It can be seen in Fig. 7 that almost all of the datapoints used in the regression agree closely

with the calculated lines within the uncertainties depicted. It is likely that the largest source of uncertainty contributing to discrepancies is associated with the pH_{ZPC} value used to compute $\log K_M^\theta$ with Eqs. (11)–(13).

It can also be seen in Fig. 7 that the slopes and intercepts of the lines vary systematically with the type of cation. For any particular reaction, the metal with the smaller crystallographic radius is associated with a shallower slope and a smaller intercept. It will be shown below that these trends can be understood and predicted for other alkaline earths using a combination of Born solvation theory and empirical radius correlations. The systematic variations were used in the case of the reaction producing $(>SOH)_2(> SO^-)_2$

_M^{2+} species in Fig. 7 and Table 2 in order to define the additional parameter B_M for M = Mg, Sr, Ba, and Ra.

3.2. Theoretical analysis of correlation slopes and intercepts

3.2.1. Interpretation of slopes with Born solvation theory

The slopes of the correlation lines depicted in Fig. 7 can be converted to values of $\Delta\Omega_{r,j}$ (see Eq. 10) which are related to individual conventional (Ω_j) and absolute ($\Omega_j^{abs.}$) solvation coefficients by

$$\Delta\Omega_{r,>SO^-\_M(OH)^+} = \Omega_{>SO^-\_M(OH)^+} - \Omega_{>SO^-}$$
$$= \Omega_{>SO^-\_M(OH)^+}^{abs.} - \Omega_{int.,>SO^-\_M(OH)^+}^{abs.} \quad (14)$$

$$\Delta\Omega_{r,tet.M(OH)^+} = \Omega_{tet.M(OH)^+} - 2\Omega_{>SO^-} - 2\Omega_{>SOH}$$
$$= \Omega_{tet.M(OH)^+}^{abs.} - \Omega_{int.,tet.M(OH)^+}^{abs.} \quad (15)$$

$$\Delta\Omega_{r,tet.M^{2+}} = \Omega_{tet.M^{2+}} - 2\Omega_{>SO^-} - 2\Omega_{>SOH}$$
$$= \Omega_{tet.M^{2+}}^{abs.} - \Omega_{int.,tet.M^{2+}}^{abs.}, \quad (16)$$

where the subscripts tet.M(OH)$^+$ and *tet*.M^{2+} refer to the species $(>SOH)_2(>SO^-)_2\_M(OH)^+$ and $(>SOH)_2(>SO^-)_2\_M^{2+}$, respectively. The absolute Born coefficients for the jth surface species (i.e., $\Omega_{>SO^-\_M(OH)^+}^{abs.}$, $\Omega_{tet.M(OH)^+}^{abs.}$, and $\Omega_{tet.M^{2+}}^{abs.}$) are related to their conventional counterparts (Sverjensky, 2005) by

$$\Omega_j = \Omega_j^{abs.} - \Omega_{>SOH}^{abs.} \quad (17)$$

which is based on the convention that

$$\Omega_{>SOH} = 0.0. \quad (18)$$

The coefficients $\Omega_{int.,>SO^-\_M(OH)^+}^{abs.}$, $\Omega_{int.,tet.M(OH)^+}^{abs}$, and $\Omega_{int.,tet.M^{2+}}^{abs}$ represent empirically determined intercepts characteristic of the adsorbed species (see below).

Definitions of absolute and conventional Born coefficients are necessary to provide a basis for relating experimentally accessible quantities to absolute solvation coefficients calculated with Born solvation theory (Helgeson and Kirkham, 1976). In the present study, the absolute solvation coefficient of the jth surface species in Eq. (17) is calculated using

$$\Omega_j^{abs.} = \frac{\eta Z_M^2}{4R_{e,M}}, \quad (19)$$

where $R_{e,M}$ represents the effective electrostatic radius for the metal M, Z_M represents the charge on M, and $\eta = 166.027$ kcal Å mol^{-1} (Sverjensky and Sahai, 1996). In contrast with the effective electrostatic radii of aqueous species and monovalent surface complexes which can be estimated based on known crystallographic radii (Helgeson and Kirkham, 1976; Sverjensky, 2005), the effective electrostatic radii of the alkaline earths (as well as divalent transition and heavy metals, and the trivalent yttrium and the rare earths are expressed in terms of hydrated metal radii ($r_{M,hydr.}$) according to

$$R_{e,M} = r_{M,hydr.} + \gamma_j, \quad (20)$$

where γ_j represents an empirically determined constant characteristic of the adsorbed species (see below). Eq. (20) is similar to the original application of Born solvation theory to metal adsorption (James and Healy, 1972) in which the hydrated radius was approximated by adding the diameter of a water molecule to a crystallographic radius. However, in the present study, the systematic relationships for solvation coefficients involving alkaline earths with different radii required the use of hydrated metal radii. Values of $r_{M, hydr.}$ are given in Table 3. It will be shown below that the combination of Eqs. (14)–(20) can be used to explain variations in solvation behavior and to facilitate predictions for the alkaline earth cations.

Eqs. (14)–(20) imply that values of $\Delta\Omega_{r,M(OH)^+}$, $\Delta\Omega_{r,tet.M(OH)^+}$, and $\Delta\Omega_{r,tet.M^{2+}}$ will depend inversely on ion size according to

$$\Delta\Omega_{r,j} = \frac{\eta}{R_{e,M}} - \Omega_{int.j}^{abs.} = \frac{\eta}{(r_{M,hydr.} + \gamma_j)} - \Omega_{int.j}^{abs.}, \quad (21)$$

where $\Omega_{int.j}^{abs.}$ and γ_j are parameters to be determined by regression of experimentally derived values of the Born reaction coefficients ($\Delta\Omega_{r,j}$). Born reaction coefficients were calculated in the present study from the slopes of the lines in Fig. 7 and are summarized in Table 3.

It can be seen in Fig. 8 that Eq. (21) is consistent with the values of $\Delta\Omega_{r,M(OH)^+}$ (Mg^{2+}, Ca^{2+}) and $\Delta\Omega_{r,tet.M(OH)^+}$ (Ca^{2+}, Sr^{2+}) within the estimated uncertainties of about ±1.5 cal mol^{-1}. Values of $\Omega_{int.j}^{abs.}$ and γ_j are summarized in Table 3. These values were used in Eq. (21) to predict additional values of $\Delta\Omega_{r,M(OH)^+}$ and $\Delta\Omega_{r,tet.M(OH)^+}$ for all the alkaline earths. In addition, owing to the paucity of data for the tetranuclear M^{2+} reaction, it was assumed that $\Delta\Omega_{r,tet.M(OH)^+} = \Delta\Omega_{r,tet.M^{2+}}$ to make predictions of $\Delta\Omega_{r,tet.M^{2+}}$ for Be, Mg, Sr, Ba, and Ra. As a result, prediction of the slopes for the reactions shown in Fig. 7 can be made for all the alkaline earths (Table 3).

3.2.2. Correlation of intercepts with cation radius

Values of $\log K_{ii,M}''$ in Table 3 (the intercepts in Fig. 7) represent values of $\log K_M^\theta$ extrapolated to zero values of $\frac{1}{\varepsilon_S}$ and $\frac{s}{r_M}$. It is assumed that the extrapolation has removed all effects of the differences between different solids. The values of $\log K_{ii,j}''$ should therefore represent intrinsic equilibrium constants characteristic of the adsorbing cation only. They can be thought of as the equilibrium constants for cation binding to a single hypothetical oxide surface characterized by $\frac{1}{\varepsilon_S}$ and $\frac{s}{r_M}$ values of zero. Under these circumstances, it seems reasonable to expect a close correlation with a property of the M^{2+} cation such as the crystallographic radius ($r_{cryst.,M}$).

It can be seen in Fig. 9 that close correlations exist for the values of $\log K_{ii,j}''$ with $r_{cryst.,M}$ consistent with the equations

$$\log K_{ii,>SO^-\_M(OH)^+}'' = 1.482 r_{cryst.,M} + 10.14, \quad (22)$$

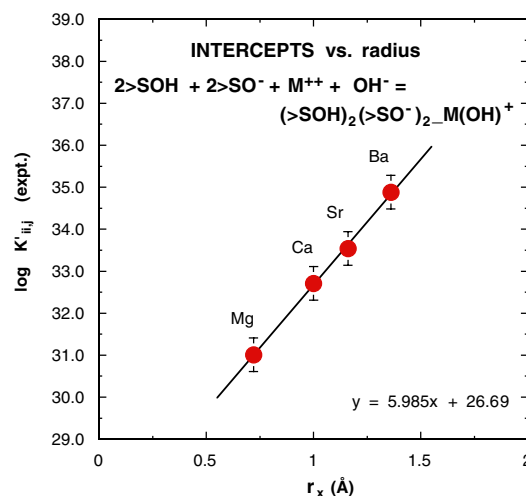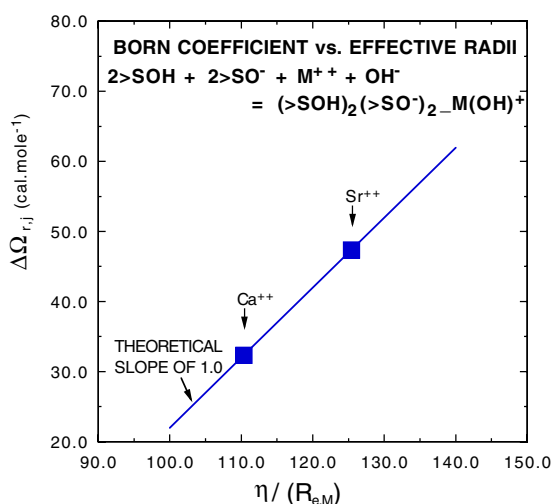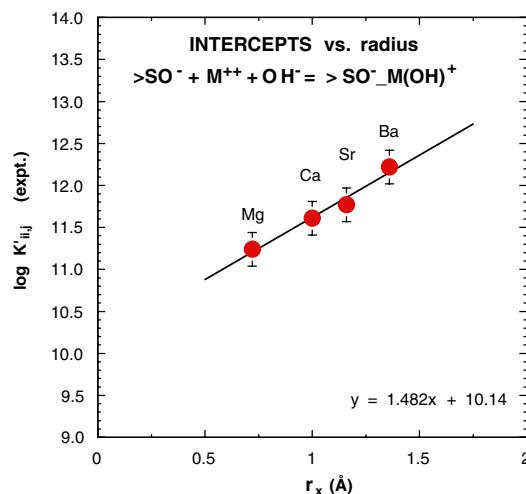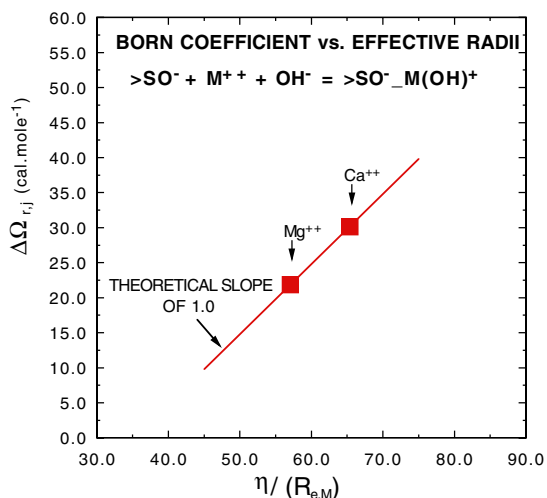$$\log K_{ii,tet.M(OH)^+}'' = 5.985 r_{cryst.,M} + 24.69, \quad (23)$$

Fig. 8. Values of the Born solvation coefficient of the reaction forming the jth surface complex ($\Delta\Omega_{r,j}$) calculated from the slopes in Fig. 7 (Table 3) versus the inverse of the effective electrostatic radius of the adsorbing cation ($\eta/R_{e.\ M}$). The solid lines with slope 1.0 are consistent with Eq. (21) and the values for γ_j, $\Omega_{int.j}^{abs.}$ given in Table 3.

and
$$\log K''_{ii,\text{tet.}\ M^{2+}} = 4.429 r_{\text{cryst.,M}} + 23.28. \qquad (24)$$

Eqs. (22)–(24) enable prediction of additional values of $\log K''_{ii,j}$ for all the alkaline earths (see Table 3). These predicted values are the intercepts of lines such as those in Fig. 7. Because both the intercepts and the slopes of lines such as those in Fig. 7 can now be predicted for all the alkaline earths, it follows that prediction of equilibrium constants for alkaline earth adsorption onto oxides can be made in the absence of any experimental data.

4. Prediction of alkaline earth metal adsorption

4.1. Prediction of equilibrium constants

Eq. (10) and the predicted coefficients in Table 3 permit the estimation of the equilibrium constants for adsorption of any alkaline earth cation on any oxide. The results are
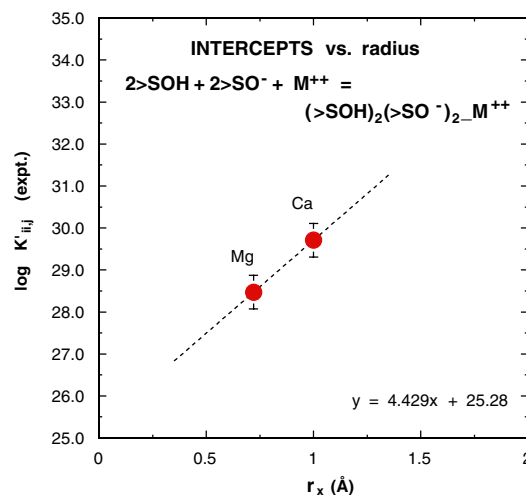
Fig. 9. Values of the intercepts ($\log K''_{ii,j}$) from Fig. 7 (Table 3) versus the crystallographic radius of the adsorbing cation ($r_{x,\ M}$). The solid lines represent regression of the data consistent with Eqs. (22)–(24).

given in Tables 4–6. Uncertainties in the predicted values of $\log K_M^\theta$ are at least ± 0.3. It should perhaps be emphasized that the values of $\log K_M^\theta$ listed in Tables 4–6 refer to standard states independent of the characteristics of

Table 4
Predicted values of $\log K^\theta_{>SO^-\_M(OH)^+}$ where M^{2+} represents a divalent cation at the β plane of the triple-layer model[a]

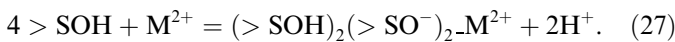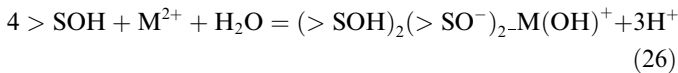| Solid	ϵ_s[b]	$\log K^\theta_{>SO^-\_M(OH)^+}$ for the reaction $>SO^- + M^{2+} + OH^- = >SO^-\_M(OH)^+$					
		Be^{2+}	Mg^{2+}	Ca^{2+}	Sr^{2+}	Ba^{2+}	Ra^{2+}
Fe_3O_4	1000	10.8	11.2	11.6	11.8	12.1	12.2
α-MnO_2	1000	10.8	11.2	11.6	11.8	12.1	12.2
α-TiO_2	121	10.7	11.1	11.4	11.6	11.9	11.9
β-TiO_2	18.6	10.3	10.3	10.4	10.5	10.5	10.4
FeOOH	15	10.2	10.1	10.1	10.1	10.1	10.0
Fe_2O_3[c]	12	10.1	9.9	9.8	9.7	9.6	9.4
α-Al_2O_3	10.4	10.0	9.7	9.5	9.4	9.2	9.0
γ-Al_2O_3	10.4	10.0	9.7	9.5	9.4	9.2	9.0
$Al(OH)_3$	8.4	9.8	9.3	9.0	8.8	8.5	8.2
α-SiO_2	4.6	8.9	7.7	6.8	6.3	5.5	4.9
am. SiO_2[d]	3.8	8.5	7.0	5.8	5.1	4.1	3.4

[a] Calculated with Eq. (10) and predicted values of $\Delta\Omega_{r,M}$ and $\log K''_{ii,M}$ from Table 3.
[b] Dielectric constant of the solid (Sverjensky, 2005).
[c] Hematites with different values of pH_{ZPC} are not treated differently here because the repulsion parameter $B_M = 0$ for this reaction.
[d] DeGussa Aerosil amorphous silicas are not treated differently from other amorphous silicas here because the repulsion parameter $B_M = 0$ for this reaction.

the actual sample and to reactions involving adsorption onto the charged species $>SO^-$. However, in practice, most studies of surface charge still employ values of $\log^* K^0_M$ referring to the hypothetical 1.0 M standard state and reactions involving $>SOH$ such as

$$> SOH + M^{2+} + H_2O => SO^-\_M(OH)^+ + 2H^+ \quad (25)$$

$$4 > SOH + M^{2+} + H_2O = (> SOH)_2(> SO^-)_2\_M(OH)^+ + 3H^+ \quad (26)$$

$$4 > SOH + M^{2+} = (> SOH)_2(> SO^-)_2\_M^{2+} + 2H^+. \quad (27)$$

Predicted values of $\log^* K^0_M$ for these reactions can be calculated from the values of $\log K^\theta_M$ in Tables 4–6 with values of the pH_{ZPC} and ΔpK^θ_n (Table 1 and Sverjensky, 2005),

together with values of the site density (N_s) and BET surface area (A_s), using

$$\log^* K^0_{>SO^-\_M(OH)^+} = \log K^\theta_{>SO^-\_M(OH)^+} - pH_{ZPC}$$
$$- \frac{\Delta pK^\theta_n}{2} - \log\left(\frac{N_s A_s}{N^\ddagger A^\ddagger}\right) - 14.0, \quad (28)$$

$$\log^* K^0_{tet.M(OH)^+} = \log K^\theta_{tet.M(OH)^+} - 2pH_{ZPC} - \Delta pK^\theta_n$$
$$- \log\left(\frac{(N_s A_s)^4}{N^\ddagger A^\ddagger} C_s^3\right) - 14.0, \quad (29)$$

$$\log^* K^0_{tet.M^{2+}} = \log K^\theta_{tet.M^{2+}} - 2pH_{ZPC} - \Delta pK^\theta_n$$
$$- \log\left(\frac{(N_s A_s)^4}{N^\ddagger A^\ddagger} C_s^3\right), \quad (30)$$

where standard state values of the site density and surface area are $N^\ddagger = 10$ sites nm^{-2} and $A^\ddagger = 10$ m^2 g^{-1}, respectively, for all solids.

Overall uncertainties in the calculated values of $\log^* K^0_M$ will reflect the uncertainties in the predicted values of $\log K^\theta_M$ as well as the uncertainties in the pH_{ZPC} value of the sample of interest. In fact, it can be seen in Eqs. (29) and (30) that values of $\log^* K^0_M$ for the tetranuclear species depend on $2pH_{ZPC}$, and are therefore especially sensitive to the accuracy of the pH_{ZPC}. The value of the pH_{ZPC} input to Eqs. (28)–(30) should not be a point-of-zero-salt effect (pH_{PZSE}), because such values are generally dependent on the type of electrolyte. Even when experimental proton titration curves for different ionic strengths intersect at a single point, the pH_{PZSE} can be 0.2–0.5 different from a pristine point-of-zero charge (Sverjensky, 2005). Ideally, a low ionic strength ($I \leqslant 0.01$) isoelectric point (IEP) should be used. However, in the absence of an experimental value, the IEP can readily be estimated from an experimental value of the pH_{PZSE} using the equation

Table 5
Predicted values of $\log K^\theta_{tet.M(OH)^+}$ where M^{2+} represents a divalent cation at the β plane of the triple-layer model[a]

Solid	$\log K^\theta_{tet.M(OH)^+}$ for the reaction $2>SOH + 2>SO^- + M^{2+} + OH^- = (>SOH)_2(>SO)^-\_M(OH)^+ + 2H^+$					
	ϵ_s[b]	Be^{2+}	Mg^{2+}	Ca^{2+}	Sr^{2+}	Ba^{2+}	Ra^{2+}
Fe_3O_4	1000	29.4	31.0	32.6	33.6	34.8	34.9
α-MnO_2	1000	29.4	31.0	32.6	33.6	34.8	34.9
α-TiO_2	121	29.4	30.9	32.5	33.3	34.4	34.5
β-TiO_2	18.6	29.4	30.6	31.4	31.8	32.0	31.6
FeOOH	15	29.4	30.5	31.1	31.3	31.4	30.8
Fe_2O_3[c]	12	29.4	30.4	30.7	30.7	30.5	29.8
α-Al_2O_3	10.4	29.4	30.3	30.4	30.3	29.8	29.0
γ-Al_2O_3	10.4	29.4	30.3	30.4	30.3	29.8	29.0
$Al(OH)_3$	8.4	29.4	30.1	29.8	29.5	28.6	27.5
α-SiO_2	4.6	29.4	29.3	27.5	26.1	23.5	21.4
am. SiO_2[d]	3.8	29.4	29.0	26.4	24.5	21.1	18.5

[a] Calculated with Eq. (10) and predicted values of $A\Omega_{rM}$ and $\log K''_{ii,M}$ from Table 3.
[b] Dielectric constant of the solid (Sverjensky, 2005).
[c] Hematites with different values of pH_{ZPC} are not treated differently here because the repulsion parameter $B_M = 0$ for this reaction.
[d] DeGussa Aerosil amorphous silicas are not treated differently from other amorphous silicas here because the repulsion parameter $B_M = 0$ for this reaction.

Table 6
Predicted values of $\log K^{\theta}_{\text{tet},M^{2+}}$ where M^{2+} represents a divalent cation at the β plane of the triple-layer model[a]

Solid	ϵ_s[b]	s/r_M[c]	$\log K^{\theta}_{\text{tet},M^{2+}}$ for the reaction $2>SOH + 2>SO^- + M^{2+} = (>SOH)_2(>SO)^-\_M^{2+} + 2H^+$					
			Be^{2+}	Mg^{2+}	Ca^{2+}	Sr^{2+}	Ba^{2+}	Ra^{2+}
Fe_3O_4	1000	0.109	12.8	22.6	26.9	29.4	30.8	31.2
α-MnO_2	1000	0.182	3.1	18.7	25.0	28.7	30.5	31.0
α-TiO_2	121	0.179	3.5	18.8	24.9	28.5	30.2	30.6
β-TiO_2	18.6	0.179	3.5	18.5	23.9	26.9	27.8	27.7
FeOOH	15	0.0508	20.5	25.2	26.8	27.6	27.6	27.2
Fe_2O_3[d]	12	0.0679	18.2	24.2	26.0	26.9	26.7	26.1
Fe_2O_3[e]	12	0.133	9.6	20.7	24.3	26.3	26.4	25.9
α-Al_2O_3	10.4	0.0753	17.3	23.7	25.5	26.4	26.0	25.2
γ-Al_2O_3	10.4	0.0753	17.3	23.7	25.5	26.4	26.0	25.2
$Al(OH)_3$	8.4	0.0754	17.2	23.5	25.0	25.6	24.8	23.8
α-SiO_2	4.6	0.126	10.5	20.0	21.3	21.7	19.5	17.5
am. SiO_2[f]	3.8	0.134	9.4	19.3	20.0	20.1	17.1	14.6
am. SiO_2[g]	3.8	0.191	1.9	16.2	18.6	19.6	16.8	14.5

[a] Calculated with Eq. (10) and predicted values of $\Delta\Omega_{rM}$ and $\log K''_{ii,M}$ from Table 3.
[b] Dielectric constant of the solid (Sverjensky, 2005).
[c] Repulsion parameter in Eq. (10). Ratio of the Pauling bond strength (s) to the distance (r_M) between the near surface metal cation of the solid and the adsorbing metal (M). Because the latter is placed on the β plane in the present paper, where the electolyte cation adsorbs, it is assumed that s/r_M can be approximated by the values derived previously for Na-salts (Sverjensky, 2005).
[d] Hematites with $pH_{ZPC} = 8.4$–8.6.
[e] Hematites with $pH_{ZPC} = 9.0$–9.5 (intensively cleaned).
[f] DeGussa Aerosil amorphous silicas.
[g] Other amorphous silicas including Cabosil.

$$pH_{PZC} = IEP = pH_{PZSE} - 0.5(\log K^{\theta}_{L^-} - \log K^{\theta}_{M^+}) \quad (31)$$

together with predicted values of $\log K_{M^+}{}^{\theta}$ and $\log K_{L^-}{}^{\theta}$ for the background electrolyte ML (Sverjensky, 2005). Eq. (31) corrects values of the pH_{PZSE} determined from the intersection of proton titration curves for electrolyte effects.

4.2. Predicted trends in adsorption with type of metal and solid

The equilibrium constants for the reactions producing the surface species $>SO^-\_M(OH)^+$ and $(>SOH)_2(>SO^-)_2\_M(OH)^+$ in Tables 4 and 5 illustrate the predicted trends established in the present study. They are shown in Fig. 10 as a function of cation type and type of solid (expressed by the inverse dielectric constant of the solid). It can be seen in the figure that for any given cation, the equilibrium constants decrease with decreasing dielectric constant. In addition, on rutile and similar solids with high dielectric constants, the equilibrium constants increase with increasing alkaline earth crystallographic radii in the sequence $Be^{2+} < Mg^{2+} < Ca^{2+} < Sr^{2+} < Ba^{2+} < Ra^{2+}$. In contrast, on hematite, gibbsite, quartz, and amorphous silica, with low dielectric constants, the equilibrium constants increase in the sequence $Ra^{2+} < Ba^{2+} < Sr^{2+} < Ca^{2+} < Mg^{2+} < Be^{2+}$. These predicted sequences are consistent with a range of data for adsorption affinities summarized in the literature. For example, the predicted sequence on high dielectric constant minerals is consistent with studies of rutile and manganese dioxide (summarized in Brown and Parks, 2001). Likewise the predicted sequence on low dielectric constant minerals is consistent with data showing that

adsorption on hematite increases in the sequence $Ba^{2+} < Sr^{2+} < Ca^{2+} < Mg^{2+}$ (Breeuwsma and Lyklema, 1973) and that adsorption on amorphous silica increases in the sequence $Ba^{2+} < Sr^{2+} < Ca^{2+}$ at pH < 7 (Karlsson et al., 2001; Dove and Craven, pers. comm.).

The adsorption affinity sequences discussed above can be explained with reference to a modified form of Eq. (10). Omitting the repulsion term results in

$$\log K^{\theta}_M = \frac{-\Delta\Omega_{r,M}}{2.303RT}\left(\frac{1}{\varepsilon_s}\right) + \log K''_{ii,M}. \quad (32)$$

The first term on the right-hand side of Eq. (32) results from Born solvation theory. This term is negligable for solids with high dielectric constants such as rutile, magnetite, and manganese dioxide. Consequently, the predicted equilibrium constants for these solids vary according to the ion-intrinsic term $\log K''_{ii,M}$ which increases with increasing crystallographic radius. It is interesting to note that this trend is opposite to that for the alkali cations (Sverjensky, 2005).

For low dielectric constant solids (e.g., quartz and amorphous silica), the solvation term in Eq. (32) becomes substantial. From Born solvation theory, values of $\Delta\Omega_{r,M}$ vary inversely with hydrated radii (Table 3). Consequently, the ion with the largest hydrated radius (Be^{2+}) produces the lines in Fig. 10 with the shallowest slopes. In contrast, the ion with the smallest hydrated radius (Ra^{2+}) produces the lines in Fig. 10 with the steepest slopes. As a result, Be^{2+} is predicted to be the strongest adsorbing alkaline earth on solids such as silica, and Ra^{2+} the weakest. These predictions should have significant consequences for the interfacial geochemistry of radium: it should show extreme
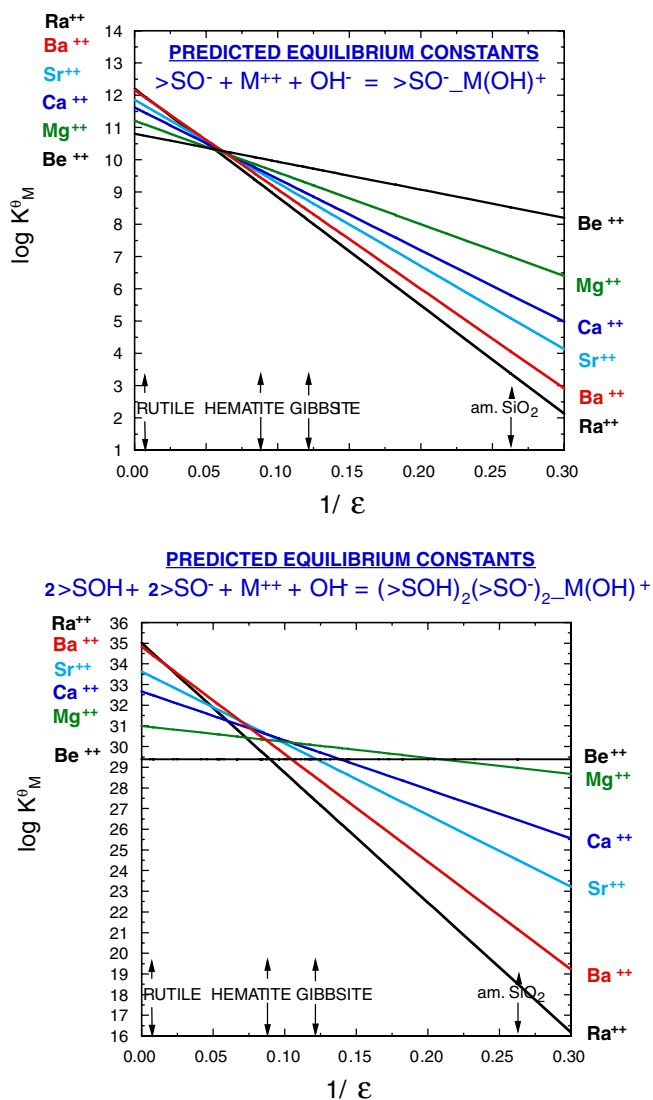
PREDICTED EQUILIBRIUM CONSTANTS

$> SO^- + M^{++} + OH^- = > SO^-\_M(OH)^+$

PREDICTED EQUILIBRIUM CONSTANTS

$2 > SOH + 2 > SO^- + M^{++} + OH^- = (> SOH)_2 (> SO^-)_2\_M(OH)^+$

Fig. 10. Predicted values of $\log K_M^{\theta}$ from Tables 4 and 5 as a function of the inverse of the dielectric constant of the solid. The predicted adsorption strengths of the alkaline earths show reverse sequences for high dielectric constant versus low dielectric constant solids because of correlations with radius versus solvation effects (see text).

differences in adsorption strength between geochemically important oxides such as manganese dioxide and silica.

To summarize, the solvation theory in Eq. (32) indicates that when alkaline earths adsorb onto high dielectric constant solids, there is essentially no opposing solvation energy involved. It is then easy for the waters of solvation on the alkaline earths to be removed as they approach the surface. If so, it is expected that alkaline earths will form inner-sphere complexes on solids such as rutile, as has been demonstrated for Sr with X-ray standing-wave studies (Fenter et al., 2000) and for Sr and Ca with molecular dynamics calculations (Predota et al., 2004b). In contrast, when alkaline earths adsorb on solids with low dielectric constants, such as goethite and silica, there is a very significant opposing free energy of solvation. This is expected to make it much more difficult to remove waters of solvation

from alkaline earths near the surface. Consequently, it is expected that alkaline earths will form outer-sphere complexes on such solids. This inference is consistent with the results of some EXAFS studies of Sr on goethite, amorphous silica, and amorphous ferric hydroxide (Axe et al., 1998; Sahai et al., 2000). It is not consistent with other EXAFS results for Sr^{2+} on goethite (Collins et al., 1998). However, it is possible that different goethites have very different surface properties. For example, the triple-layer model capacitance C_1 for goethites varies widely in a correlation with the BET surface area (Sverjensky, 2005).

5. Concluding remarks

In the present study, X-ray standing wave results for Sr^{2+} (Fenter et al., 2000; Zhang et al., 2004a,b) are used as constraints for all the alkaline earths in surface complexation simulations of proton surface charge, metal adsorption, and electrokinetic experiments. Emphasis was placed on experiments referring to a wide range of pH, ionic strength, surface coverage, and types of solids. The goal of the simulations was to determine the simplest appropriate metal adsorption reactions consistent with the X-ray studies and their state of protonation. The overall goal of the study was to analyze the systematics of equilibrium constant variation by type of cation and solid in order to be able to make predictions. Interpretation and correlation of the equilibrium constants were made with the aid of crystal–chemical, electrostatic, and thermodynamic theory. The results of the present study permit the following generalizations:

(1) A combination of reaction stoichiometries involving tetranuclear and mononuclear species can account for surface protonation, adsorption, and electrokinetic data for alkaline earth adsorption on a range of oxides and over very wide ranges of pH, ionic strength, and surface coverage. Systematic trends with cation type exist for the proportions of tetranuclear to mononuclear species. For example, on rutile, the tetranuclear reaction of the type

$$4 > SOH + M^{2+} + H_2O = (> SOH)_2 (> SO^-)_2 M(OH)^+ + 3H^+$$

predominates for the large cations Sr^{2+} and Ba^{2+} (and presumably Ra^{2+}), consistent with the X-ray results for Sr^{2+} (Fenter et al., 2000). In contrast, the mononuclear reaction
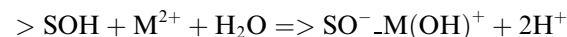
$$> SOH + M^{2+} + H_2O => SO^-\_M(OH)^+ + 2H^+$$

predominates for the much smaller Mg^{2+} (and presumably Be^{2+}), with minor amounts of the tetranuclear reaction. Both reaction types appear to be important for the intermediate size Ca^{2+} ion, with the proportions varying systematically as a function of pH, ionic strength, and surface coverage. The mononuclear reaction is predicted to be more important at higher ionic strength and surface coverage.

Similar trends to the above were apparent in analyzing adsorption data for goethite and alumina. Although, no X-ray standing-wave studies of Mg^{2+} or Ca^{2+} are available for comparison with the above results, interpretation of molecular dynamics calculations for Zn^{2+} and Ca^{2+} (Predota et al., 2004b) suggest that small ions such as Zn^{2+} (and Mg^{2+}?), bind differently than larger ions such as Ca^{2+} and Sr^{2+} at the rutile (110) surface, which is consistent with the results of the present study. However, X-ray standing wave studies of Zn^{2+} indicate a combination of two surface species, a binuclear and a mononuclear species, which differs from the results for Mg^{2+} in the present study for which mononuclear and minor tetranuclear reactions were preferred. Additional X-ray studies of the smaller (lighter) alkaline earths would provide a test of the results of the present study, as well as helping to resolve whether ion size alone is an adequate predictor of surface coordination mode.

(2) Equilibrium constants for alkaline earth adsorption expressed relative to site-occupancy standard states can be correlated, explained, and predicted with the aid of Born solvation and crystal–chemical theory. This has enabled estimation of the equilibrium constants of adsorption of Be^{2+}, Mg^{2+}, Ca^{2+}, Sr^{2+}, Ba^{2+}, and Ra^{2+} on all oxides. The results for selected reactions show specific trends with the type of cation and solid. On rutile and similar solids with high dielectric constants, the solvation contribution opposing adsorption is negligable, ion adsorption correlates directly with crystal radius. As a result, the equilibrium constants increase in the sequence $Be^{2+} < Mg^{2+} < Ca^{2+} < Sr^{2+} < Ba^{2+} < Ra^{2+}$. In contrast, on low dielectric constant solids, such as hematite, gibbsite, quartz, and amorphous silica, the solvation contribution opposing adsorption is substantial. The magnitude of the contribution is largest for ions with the smallest hydrated radii. As a result, the equilibrium constants increase in the sequence $Ra^{2+} < Ba^{2+} < Sr^{2+} < Ca^{2+} < Mg^{2+} < Be^{2+}$. Solids with intermediate values of dielectric constant, e.g., some iron oxides, may show either sequence or essentially no sequence, depending on the dielectric constant of the solid, because the magnitude of the solvation contribution is essentially cancelled out by the opposing crystallographic radius trend. These predicted sequences are consistent with a range of data for adsorption affinities summarized in the literature (e.g., in Brown and Parks, 2001).

(3) Interpretation of the above trends suggests that on high dielectric constant solids, the lack of solvation energy opposing adsorption makes it possible for the waters of solvation on an alkaline earth cation to be removed during adsorption, thereby permitting a close approach to the surface as an inner-sphere complex. This inference is consistent with the X-ray and molecular dynamics studies for Sr^{2+} and Ca^{2+}

summarized in Zhang et al. (2004b). In contrast, on low dielectric constant solids, the strong solvation energy opposing adsorption should make it difficult to remove the waters of solvation during adsorption, resulting in outer-sphere complexes. This inference is consistent with some EXAFS studies of Sr^{2+} adsorption on goethite and amorphous silica (Sahai et al., 2000). It is not consistent with other EXAFS results for Sr^{2+} on goethite (Collins et al., 1998). However, it is possible that different goethites have very different surface properties (Sverjensky, 2005).

(4) General prediction of proton surface charge for oxides in alkaline earth solutions, as well as prediction of the adsorption of alkaline earths on oxides can be made based on the results of the present study. Such predictions and the model surface speciation resulting from the present study should be directly tested with further X-ray spectroscopic studies on a variety of oxides. In combination with previously published results for oxides in 1:1 electrolytes (Sverjensky, 2005), the present study enables the predictive use of the triple-layer model for 1:1 and 2:1 electrolytes, and mixtures of these. For example, it is now possible to predict proton surface charge and adsorption on oxides in Na-K-Mg-Ca-Cl solutions for comparison with experimental data in mixed electrolyte solutions. Such calculations will provide a significant test of the predictive capabilities of the triple-layer model. In combination with similar predictive capabilities in progress for sulfate and carbonate-bearing systems, it will soon become possible to carry out calculations more relevent to natural water compositions than previously possible.

Associate editor: Donald L. Sparks

Appendix A

A.1. Nomenclature used for equilibrium constants—a summary

$^*K_M^0$ refers to a reaction of M^{2+} adsorbing onto $>SOH$ and the hypothetical 1.0 M standard state for surface species

$^*K_M^\theta$ refers to a reaction of M^{2+} adsorbing onto $>SOH$ and the site-occupancy standard states for surface species

K_M^0 refers to a reaction of M^{2+} adsorbing onto $>SO^-$ and the hypothetical 1.0 M standard state for surface species

K_M^θ refers to a reaction of M^{2+} adsorbing onto $>SO^-$ and the site-occupancy standard states for surface species

Many studies still use the hypothetical 1.0 M standard state for surface species. However, equilibrium constants on this basis include a dependence on site density, surface area, and in some instances, solid concentration. Such equilibrium constants for different samples of the same solid, or different solids, cannot be sensibly compared (Sverjensky, 2003). In order to be able to compare, correlate, and predict equilibrium constants for surface species, it is essential to use an internally consistent set of surface protonation, electrolyte adsorption, and metal adsorption equilibrium constants referring to standard states independent of site densities, surface areas, and solid concentrations. The site-occupancy standard states described below were developed for this purpose. Equations for the conversion from the hypothetical 1.0 M standard state to the site-occupancy standard states are also summarized below.

A.2. Standard states used in the present study

Equilibrium constants in the present study written with the superscript "θ", e.g., K^θ, refer to site-occupancy standard states (Sverjensky, 2003). They can be summarized as follows. The standard state for sorbent sites ($>SOH$) refers to unit activity of surface sorption sites on a completely unsaturated surface at any P and T such that

$$a_{>SOH} = \lambda_{>SOH}X_{>SOH} \tag{A.1}$$

and $\lambda_{>SOH} \to 1$ as $X_{>SOH} \to 1$. In these relations, $a_{>SOH}$, $\lambda_{>SOH}$, and $X_{>SOH}$ represent the activity, activity coefficient, and mole fraction of $>SOH$ sites, respectively. This is, in principle, a physically achievable standard state. For any sorbate species ($>j$), the standard state refers to unit activity of surface species on a completely saturated surface with zero potential at any P and T referenced to infinite dilution, expressed by

$$a_{>j} = \lambda_{>j}X_{>j}, \tag{A.2}$$

where $\lambda_{>j} \to 1$ and the "ψ term" in the electrochemical potential equation for $>j$ approaches zero as $X_{>j} \to 0$. As above, $a_{>j}$, $\lambda_{>j}$, and $X_{>j}$ represent the activity, activity coefficient, and mole fraction of the $>j$th sorbate species, respectively. This is a hypothetical standard state, i.e., not physically achievable.

An advantage of defining the standard states for sorbent sites and sorbate species in this way is that in model calculations the limiting conditions of $X_{>SOH} \to 1$ and $X_{>j} \to 0$ are often approached. In other words, for the triple-layer model used here, $>SOH$ is commonly by far the dominant species, whereas sorbates such as $>SOH_2^+$, $>SOH_2^+\_NO_3^-$,

and $>SO^-\_M(OH)^+$ are often minor species. Under these circumstances, it is reasonable to assume that $\lambda_{>SOH} \approx 1$ and $\lambda_{>j} \approx 1$.

For the surface protonation reactions

$$> SOH + H^+ => SOH_2^+$$

$$> SO^- + H^+ => SOH$$

$$> SO^- + 2H^+ => SOH_2^+$$

$$> SO^- + > SOH_2^+ = 2 > SOH$$
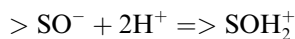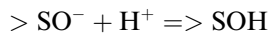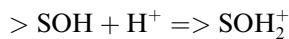
the standard states adopted above are related to the widely used hypothetical 1.0 M standard state (written with a superscript "0", Sverjensky, 2003) by

$$K_1^\theta = K_1^0 \left(\frac{N_sA_s}{N^\ddagger A^\ddagger}\right) \tag{A.3}$$

$$K_2^\theta = K_2^0 \left(\frac{N_sA_s}{N^\ddagger A^\ddagger}\right)^{-1} \tag{A.4}$$

$$K_{ZPC}^\theta = K_{ZPC}^0 \tag{A.5}$$

and

$$K_n^\theta = K_n^0 \left(\frac{N_sA_s}{N^\ddagger A^\ddagger}\right)^{-2} \tag{A.6}$$

respectively,
where

N_s represents the surface site density on the sth solid sorbent (sites m^{-2}),
$N^\ddagger$ represents the standard state sorbate species site density (sites m^{-2}),
A_s represents the BET surface area of the sth solid sorbent ($m^2\ g^{-1}$),
$A^\ddagger$ represents a standard state BET surface area ($m^2\ g^{-1}$).

In the present study, values of $N^\ddagger = 10 \times 10^{18}$ sites m^{-2} and $A^\ddagger = 10\ m^2\ g^{-1}$ are selected for all solids. It is emphasized that these values are properties of the hypothetical standard state applicable to all samples of all solids.

Equilibria for adsorption of the monovalent electrolyte ions M^+ and L^- can be expressed by

$$> SOH + M^+ => SO^-\_M^+ + H^+ \tag{A.7}$$

and

$$> SOH + H^+ + L^- => SOH_2^+\_L^- \tag{A.8}$$
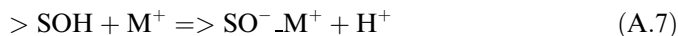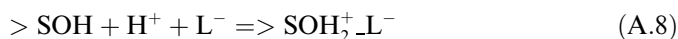
for which

$$^*K_{M^+}^\theta = {}^*K_{M^+}^0 \left(\frac{N_sA_s}{N^\ddagger A^\ddagger}\right) \tag{A.9}$$
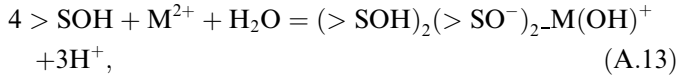
and

$$^*K_{L^-}^\theta = {}^*K_{L^-}^0 \left(\frac{N_sA_s}{N^\ddagger A^\ddagger}\right). \tag{A.10}$$

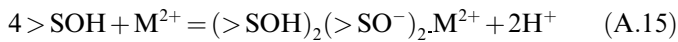Equilibria for adsorption of divalent alkaline earth cations used in the present study can be expressed by

$$> SOH + M^{2+} + H_2O => SO^-\_M(OH)^+ + 2H^+, \quad (A.11)$$

where

$$^*K^\theta_{>SO^-\_M(OH)^+} = \left(\frac{a_{>SO^-\_M(OH)^+}a_{H^+}^2}{a_{>SOH}a_{M^{2+}}a_{H_2O}}\right)10^{\frac{F(\psi_\beta-\psi_0)}{2.303RT}}, \quad (A.12)$$

$$4 > SOH + M^{2+} + H_2O = (> SOH)_2(> SO^-)_2\_M(OH)^+ \\ + 3H^+, \quad (A.13)$$

where

$$^*K^\theta_{(>SOH)_2(>SO^-)_2\_M(OH)^+}$$
$$= \left(\frac{a_{(>SOH)_2(>SO^-)_2\_M(OH)^+}a_{H^+}^3}{a_{>SOH}^4 a_{M^{2+}} a_{H_2O}}\right)10^{\frac{F\left(\psi_\beta-2\psi_0\right)}{2.303RT}} \quad (A.14)$$

and

$$4 > SOH + M^{2+} = (> SOH)_2(> SO^-)_2\_M^{2+} + 2H^+ \quad (A.15)$$

where

$$^*K^\theta_{(>SOH)_2(>SO^-)_2\_M^{2+}}$$
$$= \left(\frac{a_{(>SOH)_2(>SO^-)_2\_M^{2+}}a_{H^+}^2}{a_{>SOH}^4 a_{M^{2+}}}\right)10^{\frac{2F(\psi_\beta-\psi_0)}{2.303RT}}. \quad (A.16)$$

For these reactions the relationship to the hypothetical 1.0 M standard state is given by

$$^*K^\theta_{>SO^-\_M(OH)^+} = {^*K^0_{>SO^-\_M(OH)^+}}\left(\frac{N_s A_s}{N^\ddagger A^\ddagger}\right), \quad (A.17)$$

$$^*K^\theta_{tet.M(OH)^+} = {^*K^0_{tet.M(OH)^+}}\left(\frac{(N_s A_s)^4}{N^\ddagger A^\ddagger}C_s^3\right), \quad (A.18)$$

and

$$^*K^\theta_{tet.M^{2+}} = {^*K^0_{tet.M^{2+}}}\left(\frac{(N_s A_s)^4}{N^\ddagger A^\ddagger}C_s^3\right). \quad (A.19)$$

In Eqs. (A.18 and A.19), the dependence on site density and surface area to the 4th power is a result of the coefficient of 4>SOH in reactions A13 and A15. The dependence on solid concentration is expressed to the 3rd power because the sorbate dependence is assumed to cancel with the sorbent. This reduces the dependence for solid concentration from the 4th power to the 3rd power. The utility of these standard state conversions can be seen in the correlation graphs in Fig. 7 of the text.

References

Ahmed, S.M., Cleave, A.B.v., 1965. Adsorption and flotation studies with quartz: Part I. Adsorption of calcium, hydrogen and hydroxyl ions on quartz. *Can. J. Chem. Eng.* **43**, 23–26.

Ali, M.A., 1994. The influence of simple organic acids on sorption of inorganic ions at the goethite/water interface. Ph.D., University of Pittsburgh.

Ali, M.A., Dzombak, D.A., 1996. Effects of simple organic acids on sorption of Cu^{2+} and Ca^{2+} on goethite. *Geochim. Cosmochim. Acta* **60**, 291–304.

Auwer, C.D., Drot, R., Simoni, E., Conradson, S.D., Gailhanou, M., Mustre de Leon, J., 2003. Grazing incidence XAFS spectroscopy of uranyl sorbed onto TiO_2 rutile surfaces. *New J. Chem.* **27**, 648–655.

Axe, L., Bunker, G.B., Anderson, P.R., Tyson, T.A., 1998. An XAFS analysis of strontium at the hydrous ferric oxide surface. *J. Colloid Interface Sci.* **199**, 44–52.

Balistrieri, L.S., Murray, J.W., 1981. The surface chemistry of goethite (αFeOOH) in major ion seawater. *Am. J. Sci.* **281**, 788–806.

Bargar, J.R., Brown Jr., G.E., Parks, G.A., 1997a. Surface complexation of Pb. at oxide–water interfaces: I. XAFS and bond-valence determination of mononuclear and polynuclear Pb(II) sorption products on aluminum oxides. *Geochim. Cosmochim. Acta* **61**, 2617–2637.

Bargar, J.R., Brown Jr., G.E., Parks, G.A., 1997b. Surface complexation of Pb(II) at oxide–water interfaces: II. XAFS and bond-valence determination of mononuclear Pb(II) sorption products and surface functional groups on iron oxides. *Geochim. Cosmochim. Acta* **61**, 2639–2652.

Bargar, J.R., Towle, S.N., Brown Jr., G.E., Parks, G.A., 1997c. XAFS and bond-valence determination of the structures and compositions of surface functional groups and Pb(II) and Co(II) sorption products on single-crystal α-Al_2O_3. *J. Colloid Interface Sci.* **185**, 473–492.

Boily, J.-F., Sjöberg, S., Persson, P., 2005. Structures and stabilities of Cd and Cd-phthalate complexes at the goethite–water interface. *Geochim. Cosmochim. Acta* **69**, 3219–3236.

Breeuwsma, A., Lyklema, J., 1973. Physical and chemical adsorption of ions in the electrical double layer on hematite (α-Fe_2O_3). *J. Colloid Interface Sci.* **43**, 437–448.

Brown Jr., G.E., 1990. Spectroscopic studies of chemisorption reaction mechanisms at oxide–water interfaces. In: White, A.F. (Ed.), *Mineral–Water Interface Geochemistry*, vol. 23. Min. Soc. Am.

Brown Jr., G.E., Parks, G.A., 2001. Sorption of trace elements on mineral surfaces: modern perspectives from spectroscopic studies, and comments on sorption in the marine environment. *Int. Geol. Rev.* **43**, 963–1073.

Brown Jr., G.E., Sturchio, N.C., 2002. An overview of synchrotron radiation applications to low-temperature geochemistry and environmental science. In: Sutton, S.R. (Ed.), *Applications of Synchrotron Radiation in Low-temperature Geochemistry and Environmental Science*, vol. 49. Mineralogical Society of America, pp. 1–115.

Charmas, R., Rudzinski, W., Piasecki, W., Prelot, B., Thomas, F., Villieras, F., Janusz, W., 2002. Adsorption of cadmium ions at the electrolyte/silica interface II. Theoretical study of surface energetic heterogeneity. *Appl. Surf. Sci.* **196**, 331–342.

Cheah, S., Brown Jr., G.E., Parks, G.A., 1998. XAFS study of Cu(II) sorption on amorphous silica and γ-Al_2O_3: Effect of substrate and time on sorption complexes. *J. Colloid Interface Sci.* **208**, 110–128.

Chen, C., Hayes, K.F., 1999. X-ray absorption spectroscopy investigation of aqueous Co(II) and Sr(II) sorption. *Geochim. Cosmochim. Acta* **63**, 3205–3215.

Collins, C.R., Sherman, D.M., Ragnarsdottir, K.V., 1998. The adsorption mechanism of Sr^{2+} on the surface of goethite. *Radiochim. Acta* **81**, 201–206.

Criscenti, L.J., Sverjensky, D.A., 1999. The role of electrolyte anions ClO_4^-, NO_3^-, and Cl^- in divalent metal (M^{2+}) adsorption on oxide and hydroxide surfaces in salt solutions. *Am. J. Sci.* **299**, 828–899.

Criscenti, L.J., Sverjensky, D.A., 2002. A single-site model for divalent and heavy metal adsorption over a range of metal concentrations. *J. Colloid Interface Sci.* **253**, 329–352.

Davis, J.A., James, R.O., Leckie, J.O., 1978. Surface ionization and complexation at the oxide/water interface I. Computation of electrical double layer properties in simple electrolytes. *J. Colloid Interface Sci.* **63**, 480–499.

Davis, J.A., Kent, D.B., 1990. Surface complexation modeling in aqueous geochemistry. In: White, A.F. (Ed.), *Mineral–Water Interface Geochemistry*, vol. 23. Mineralogical Society of America, pp. 177–259.

Davis, J.A., Leckie, J.O., 1978. Surface ionization and complexation at the oxide/water interface II. Surface properties of amorphous iron oxyhydroxide and adsorption of metal ions. *J. Colloid Interface Sci.* **67**, 90–107.

Drever, J.I., 1997. *The Geochemistry of Natural Waters*. Prentice Hall, Englewood Cliffs, NJ.

Dyer, J.A., Trivedi, P., Scrivner, N.C., Sparks, D.L., 2004. Surface complexation modeling of zinc sorption onto ferrihydrite. *J. Colloid Interface Sci.* 270, 56–65.

Dzombak, D.A., Morel, F.M.M., 1990. *Surface Complexation Modeling*. John Wiley and Sons.

Felmy, A.R., Rustad, J.R., 1998. Molecular statics calculations of proton binding to goethite surfaces: thermodynamic modeling of the surface charging and protonation of goethite in aqueous solution. *Geochim. Cosmochim. Acta* 62, 25–31.

Fenter, P., Cheng, L., Rihs, S., Machesky, M., Bedyzk, M.D., Sturchio, N.C., 2000. Electrical double-layer structure at the rutile–water interface as observed in situ with small-period X-ray standing waves. *J. Colloid Interface Sci.* 225, 154–165.

Gabriel, U., Charlet, L., Schlapfer, C.W., Vial, J.C., Brachmann, A., Geipel, G., 2001. Uranyl surface speciation on silica particles studied by time-resolved laser-induced fluorescence spectroscopy. *J. Colloid Interface Sci.* 239, 358–368.

Gunneriusson, L., Sjöberg, S., 1993. Surface complexation in the H^+-goethite(α-FeOOH)-Hg(II)-chloride system. *J. Colloid Interface Sci.* 156, 121–128.

Hayes, K.F., Leckie, J.O., 1986. Mechanism of lead ion adsorption at the goethite–water interface. In: Hayes, K.F. (Ed.), *Geochemical Processes at Mineral Surfaces*, vol. 323. American Chemical Society, pp. 114–141.

Hayes, K.F., Leckie, J.O., 1987. Modeling ionic strength effects on cation adsorption at hydrous oxide/solution interfaces. *J. Colloid Interface Sci.* 115, 564–572.

Hayes, K.F., Roe, A.L., Brown Jr., G.A., Hodgson, K.O., Leckie, J.O., Parks, G.A., 1987. In situ X-ray absorption study of surface complexes: Selenium oxyanions on α-FeOOH. *Science* 238, 783–786.

Helgeson, H.C., Kirkham, D.H., 1976. Theoretical prediction of the thermodynamic properties of aqueous electrolytes at high pressures and temperatures. III. Equation of state for aqueous species at infinite dilution. *Am. J. Sci.* 276, 97–240.

Hiemstra, T., van Riemsdijk, W.H., 1996. A surface structural approach to ion adsorption: the charge distribution (CD) model. *J. Colloid Interface Sci.* 179, 488–508.

Huang, C., Stumm, W., 1973. Specific Adsorption of Cations on Hydrous γ-Al_2O_3. *Journal of Colloid and Interface Science* 43 (2), 409–420.

Hyun, S.P., Cho, Y.H., Hahn, P.S., 2003. An electron paramagnetic resonance study of Cu(II) sorbed on quartz. *J. Colloid Interface Sci.* 257, 179–187.

James, R.O., Healy, T.W., 1972. Adsorption of hydrolyzable metal ions at the oxide–water interface III. A thermodynamic model of adsorption. *J. Colloid Interface Sci.* 40, 65–81.

James, R.O., Stiglich, P.J., Healy, T.W., 1981. The TiO_2/aqueous electrolyte system – applications of collod models and model colloids. In: Tewari, P.H. (Ed.), *Adsorption From Aqueous Solutions*. Plenum, pp. 19–40.

Jang, H.M., Fuerstenau, D.W., 1986. The specific adsorption of alkaline-earth cations at the rutile/water interface. *Colloid Surface* 21, 235–257.

Karlsson, M., Craven, C., Dove, P.M., Casey, W.H., 2001. Surface charge concentrations on silica in diffferent 1.0 m metal-chloride background electrolytes and implications for dissolution rates. *Aquat. Geochem.* 7, 13–32.

Kent, D.B., Kastner, M., 1985. Mg^{2+} removal in the system Mg^{2+}-amorphous silica-H_2O by adsorption and Mg-silicate precipitation. *Geochim. Cosmochim. Acta* 49, 1123–1136.

Kitamura, A., Fujiwara, K., Yamamoto, T., Nishikawa, S., Moriyama, H., 1999. Analysis of adsorption behavior of cations onto quartz surface by electrical double-layer method. *J. Nucl. Sci. Technol.* 36, 1167–1175.

Kosmulski, M., 1994. Co-adsorption of mono- and multivalent ions on silica and alumina. *Ber. Bunsenges. Phys. Chem.* 98, 1062–1067.

Machesky, M., Wesolowski, D.J., Palmer, D.A., Ichiro-Hayashi, K., 1998. Potentiometric titrations of rutile suspensions to 250 °C. *Journal of Colloid and Interface Science* 200, 298–309.

O'Day, P.A., Newville, M., Neuhoff, P.S., Sahai, N., Carroll, S.A., 2000. X-ray adsorption spectroscopy of strontium(II) coordination I. Static and thermal disorder in crystalline, hydrated, and precipitated solids and in aqueous solution. *J. Colloid Interface Sci.* 222, 184–197.

Ostergren, J.D., Trainor, T.P., Bargar, J.R., Brown Jr., G.E., Parks, G.A., 2000. Inorganic ligand effects on Pb(II) sorption to goethite (α-FeOOH) I. Carbonate.. *J. Colloid Interface Sci.* 225, 466–482.

Peacock, C.L., Sherman, D.M., 2004. Vanadium adsorption onto goethite (α-FeOOH) at pH 1.5 to 12: a surface complexation model based on ab initio molecular geometries and EAFS spectroscopy. *Geochim. Cosmochim. Acta* 68, 1723–1733.

Predota, M., Bandura, A.V., Cummings, P.T., Kubicki, J.D., Wesolowski, D.J., Chialvo, A.A., Machesky, M., 2004a. Electric double layer at the rutile (110) surface. 1. Structure of surfaces and interfacial water from molecular dynamics by use of ab initio potentials. *J. Phys. Chem. B* 108, 12049–12060.

Predota, M., Zhang, Z., Fenter, P., Wesolowski, D.J., Cummings, P.T., 2004b. Electric double layer at the rutile (110) surface. 2. Adsorption of ions from molecular dynamics and X-ray experiments. *J. Phys. Chem. B* 108, 12061–12072.

Prélot, B., Janusz, W., Thomas, F., Villiéras, F., Charmas, R., Piasecki, W., Rudzinski, W., 2002. Adsorption of cadmium ions at the electrolyte/silica interface I. Experimental study of surface properties. *Appl. Surf. Sci.* 196, 322–330.

Ridley, M.K., Machesky, M.L., Wesolowski, D.J., Palmer, D.A., 1999. Calcium adsorption at the rutile–water interface: a potentiometric study in NaCl media to 250 °C. *Geochim. Cosmochim. Acta* 63, 3087–3096.

Ridley, M.K., Machesky, M.L., Wesolowski, D.J., Palmer, D.A., 2004. Modeling the surface complexation of calcium at the rutile–water interface to 250 °C. *Geochim. Cosmochim. Acta* 68, 239–251.

Riese, A.C., 1983. Adsorption of radium and thorium onto quartz and kaolinite: A comparison of solution/surface equilibrium models. Ph.D., Colorado School of Mines.

Rietra, R.P.J.J., Hiemstra, T., van Riemsdijk, W.H., 2001. Interaction between calcium and phosphate adsorption on goethite. *Environ. Sci. Technol.* 35, 3369–3374.

Robinson, R.A., Stokes, R.H., 1959. *Electrolyte Solutions*. Butterworths, London, 571 p.

Sahai, N., Carroll, S.A., Roberts, S., O'Day, P.A., 2000. X-ray adsorption spectroscopy of strontium(II) coordination II. Sorption and precipitation at kaolinite, amorphous silica and goethite surfaces. *J. Colloid Interface Sci.* 222, 198–212.

Sahai, N., Sverjensky, D.A., 1997a. Evaluation of internally-consistent parameters for the triple-layer model by the systematic analysis of oxide surface titration data. *Geochim. Cosmochim. Acta* 61, 2801–2826.

Sahai, N., Sverjensky, D.A., 1997b. Solvation and electrostatic model for specific electrolyte adsorption. *Geochim. Cosmochim. Acta* 61, 2827–2848.

Schindler, P.W., Stumm, W., 1987. The surface chemistry of oxides, hydroxides, and oxide minerals. In: Stumm, W. (Ed.), *Aquatic Surface Chemistry: Chemical Processes at the Particle–Water Interface*. John Wiley and Sons, pp. 83–110.

Shannon, R.D., Prewitt, C.T., 1969. Effective ionic radii in oxides and fluorides. *Acta Cryst.* B25, 925–946.

Spadini, L., Manceau, A., Schindler, P.W., Charlet, L., 1994. Structure and stability of Cd^{2+} surface complexes on ferric oxides 1. Results from EXAFS spectroscopy. *J. Colloid Interface Sci.* 168, 73–86.

Spadini, L., Schindler, P., Charlet, L., Manceau, A., Ragnarsdottir, K.V., 2003. Hydrous ferric oxide: evaluation of Cd-HFO surface complexation models combining CdK EXAFS data, potentiometric titration results, and surface site structures identified from mineralogical knowledge. *J. Colloid Interface Sci.* 266, 1–18.

Sposito, G., 1986. Distinguishing adsorption from surface precipitation. In: Hayes, K.F. (Ed.), *Geochemical Processes at Mineral Surfaces*, vol. 323. American Chemical Society, pp. 217–228.

Stumm, W., 1992. Chemistry of the solid–water interface. *John Wiley and Sons. Inc.*

Sverjensky, D.A., 1993. Physical surface-complexation models for sorption at the mineral–water interface. *Nature* **364**, 776–780 (August 26).

Sverjensky, D.A., 1994. Zero-point-of-charge prediction from crystal chemistry and solvation theory. *Geochim. Cosmochim. Acta* **58**, 3123–3129.

Sverjensky, D.A., 2001. Interpretation and prediction of triple-layer model capacitances and the structure of the oxide-electrolyte–water interface. *Geochim. Cosmochim. Acta* **65**, 3641–3653.

Sverjensky, D.A., 2003. Standard states for the activities of mineral surface-sites and species. *Geochim. Cosmochim. Acta* **67**, 17–28.

Sverjensky, D.A., 2005. Prediction of surface charge on oxides in salt solutions: revisions for 1:1 (M^+L^-) electrolytes. *Geochim. Cosmochim. Acta* **69**, 225–257.

Sverjensky, D.A., Sahai, N., 1996. Theoretical prediction of single-site surface protonation equilibrium constants for oxides and silicates in water. *Geochimica. et Cosmochimica. Acta* **60**, 3773–3798.

Tadros, T.F., Lyklema, J., 1969. The electrical double layer on silica in the presence of bivalent counter ions. *Electroanal. Chem. Interfacial Electrochem.* **22**, 1–7.

Trivedi, P., Dyer, J.A., Sparks, D.L., 2003. Lead sorption onto ferrihydrite. 1. A macroscopic and spectroscopic assessment. *Environ. Sci. Technol.* **37**, 908–914.

Venema, P., Hiemstra, T., van Riemsdijk, W.H., 1996. Multisite adsorption of cadmium on goethite. *J. Colloid Interface Sci.* **183**, 515–527.

Venema, P., Hiemstra, T., van Riemsdijk, W.H., 1997. Interaction of cadmium with phosphate on goethite. *J. Colloid Interface Sci.* **192**, 94–103.

Vuceta, J., 1976. Adsorption of Pb(II) and Cu(II) on α-quartz from aqueous solutions: influence of pH, ionic strength, and complexing ligands. Ph.D., California Institute of Technology.

Waychunas, G.A., Fuller, C.C., Davis, J.A., 2002. Surface complexation and precipitate geometry for aqueous Zn(II) sorption on ferrihydrite. I: X-ray adsorption extended fine structure spectroscopy analysis. *Geochim. Cosmochim. Acta* **66**, 1119–1137.

Weng, L.P., Koopal, L.K., Hiemstra, T., Meeussen, J.C.L., van Riemsdijk, W.H., 2005. Interactions of calcium and fulvic acid at the goethite–water interface. *Geochim. Cosmochim. Acta* **69**, 325–339.

Westall, J.C., Hohl, H., 1980. A comparison of electrostatic models for the oxide/solution interface. *Adv. Colloid Interface Sci.* **12**, 265–294.

Wiese, G.R., Healy, T.W., 1975. Coagulation and electrokinetic behavior of TiO_2 and Al_2O_3 colloidal dispersions. *J. Colloid Interface Sci.* **51**, 427–433.

Yates, D.E., 1975. The structure of the oxide/aqueous electrolyte interface. Ph.D., University of Melbourne.

Yates, D.E., James, R.O., Healy, T.W., 1980. Titanium dioxide–electrolyte interface. Part 2. Surface charge (titration) studies. *J. Chem. Soc. Faraday Trans.* **76**, 9–18.

Zhang, Z., Fenter, P., Cheng, L., Sturchio, N.C., Bedyzk, M.D., Machesky, M., Wesolowski, D.J., 2004a. Model-independent X-ray imaging of adsorbed cations at the crystal–water interface. *Surface Sci.* **554**, L95–L100.

Zhang, Z., Fenter, P., Cheng, L., Sturchio, N.C., Bedyzk, M.D., Predota, M., Bandura, A.V., Kubicki, J.D., Lvov, S.N., Cummings, P.T., Chialvo, A.A., Ridley, M.K., Benezeth, P., Anovitz, L., Palmer, D.A., Machesky, M., Wesolowski, D.J., 2004b. Ion adsorption at the rutile–water interface: linking molecular and macroscopic properties. *Langmuir* **20**, 4954–4969.